

# Abundance of density wave phases in twisted trilayer graphene on WSe<sub>2</sub>

Phum Siriviboon<sup>1\*</sup>, Jiang-Xiazi Lin<sup>1\*</sup>, Harley D. Scammell<sup>2</sup>, Song Liu<sup>3</sup>, Daniel Rhodes<sup>3</sup>,

K. Watanabe<sup>4</sup>, T. Taniguchi<sup>5</sup>, James Hone<sup>3</sup>, Mathias S. Scheurer<sup>6</sup>, and J.I.A. Li<sup>1\*</sup>

<sup>1</sup>*Department of Physics, Brown University, Providence, RI 02912, USA*

<sup>2</sup>*School of Physics, the University of New South Wales, Sydney, NSW, 2052 Australia*

<sup>3</sup>*Department of Mechanical Engineering, Columbia University, New York, NY 10027, USA*

<sup>4</sup>*Research Center for Functional Materials, National Institute for Materials Science, 1-1 Namiki, Tsukuba 305-0044, Japan*

<sup>5</sup>*International Center for Materials Nanoarchitectonics,*

*National Institute for Materials Science, 1-1 Namiki, Tsukuba 305-0044, Japan*

<sup>6</sup>*Institute for Theoretical Physics, University of Innsbruck, Innsbruck, A-6020, Austria and*

*\*These authors contributed equally in this work.*

(Dated: December 15, 2021)

The presence of different types of density-wave (DW) phases is a hallmark of the complex, intertwined phase diagram of many strongly correlated materials [1, 2], such as the cuprates superconductors. Although graphene moiré systems have been compared with high-temperature superconductors, the observation of density wave instabilities has remained rare. In this work, we report an abundance of correlated phases in twisted trilayer graphene (tTLG) with a density modulation of 1/4 and 1/2 moiré filling, which are stabilized through the proximity effect across an interface with a tungsten diselenide (WSe<sub>2</sub>) crystal. At the same time, recursive structures in the Hofstadter spectrum and symmetry-broken Chern insulators are observed in the quantum Hall regime. These observations are indicative of DW order that spontaneously breaks the translational symmetry of the moiré lattice. Notably, there is no clear hierarchy between the robustness of correlation-driven insulators at integer and fractional fillings. This is in stark contrast with graphene moiré systems where correlation-driven phenomena are the most robust when each moiré unit cell is occupied by an integer number of electrons. Taken together, our findings uncover a novel flavor of moiré physics, induced by the proximity effect across the tTLG/WSe<sub>2</sub> interface.

A handful of graphene moiré systems have been studied since the discovery of magic-angle twisted bilayer graphene [3–10]. The landscape of emergent quantum phenomena in these structures share a common thread that originates from a unique symmetry breaking mechanism. Due to strong Coulomb interaction in graphene moiré systems, charge carriers tend to spontaneously develop an isospin polarization without breaking translation symmetry, every time an integer number of electrons occupy a moiré unit cell. For simplicity, we will refer to this mechanism as translation-invariant flavor-symmetry breaking (TI-FSB), and these commensurate band fillings as integer moiré filling. For instance, TI-

FSB can lead to insulators with diverging resistance and sign changes in the Hall density. Furthermore, the cascades of band resets [11–13] can also be understood from TI-FSB. In fact, up to now, most quantum emergent phases in graphene moiré systems are believed to be directly associated with or crucially influenced by TI-FSB at integer moiré fillings, such as correlated insulators [3, 14, 15], orbital ferromagnets [7, 8, 16–18] and superconductivity [4, 9, 10, 15]. Owing to the density modulation of integer moiré filling, this can be understood, at least phenomenologically, by electronic correlations on the length scale of one moiré wavelength.

In an effort to further engineer graphene moiré systems, a new method has recently emerged utilizing the proximity effect across the atomic interface between graphene and transition metal dichalcogenides (TMD) [18, 19]. Since electron wave functions hybridize across the atomic interface, the proximity effect provides a unique route to perform complex band engineering. For example, the atomic interface between graphene and tungsten diselenide (WSe<sub>2</sub>) is widely studied as a method to endow graphene with spin-orbit interaction much larger than what is intrinsic to carbon atoms [20–26]. The strongly reduced bandwidth of small-angle graphene moiré systems, makes their physics more susceptible to the influence of proximity induced spin-orbit coupling (SOC), which may significantly alter the moiré bands, potentially giving rise to rich band topology [27]. Indeed, the interface between magic-angle twisted bilayer graphene (tBLG) and WSe<sub>2</sub> is shown to transform the isospin order at half-filled moiré band, stabilizing a ferromagnetic state with spontaneous valley polarization [18].

In this work, we uncover an abundance of correlation-driven insulators appearing with density modulation of 1/4 and 1/2 moiré filling in tTLG proximity-coupled to WSe<sub>2</sub>. The geometry of the heterostructure studied is shown in Fig. 1a. An atomic interface is created by stacking a few-layer WSe<sub>2</sub> crystal on top of tTLG with alternating twist angles between the top/middle and middle/bottom graphene layers [9, 10]. Three separate samples consisting of tTLG and WSe<sub>2</sub> are studied in this work. The tTLG in sample A, B and C have twist angle

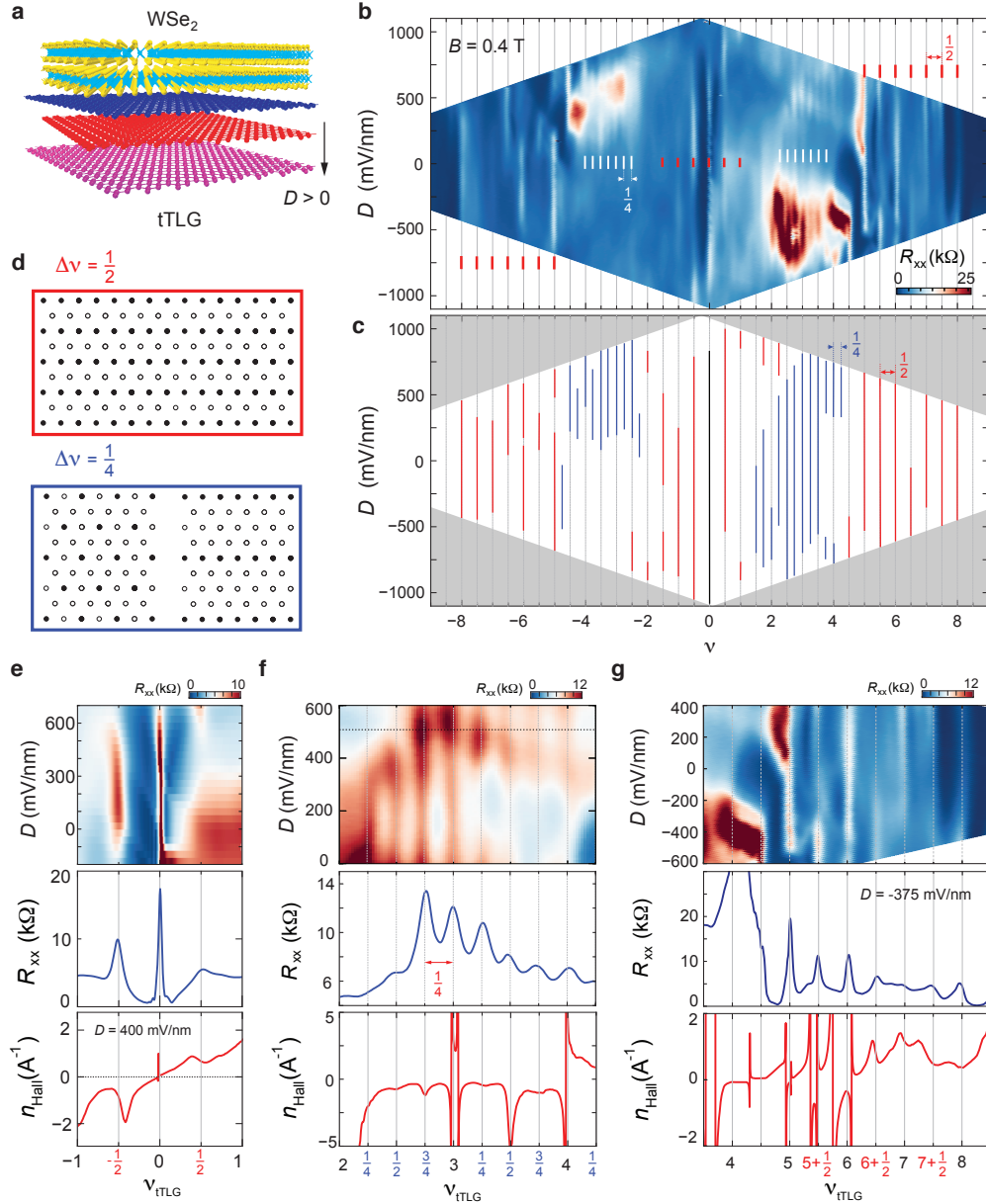


FIG. 1. **Density wave states.** (a) Schematic of the interface between WSe<sub>2</sub> and tTLG. Positive  $D$  is defined as a perpendicular electric field pointing downwards away from WSe<sub>2</sub>. (b) Longitudinal resistance  $R_{xx}$  as a function of  $D$  and moiré filling  $\nu_{tTLG}$  measured at  $B = 0.4$  T and  $T = 20$  mK. (c) Schematic for the  $\nu_{tTLG} - D$  phase diagram where the location for resistive peaks are marked by solid red and blue lines. Both blue and red lines track constant moiré filling  $\nu_{tTLG}$ . Blue (red) lines emerge with a periodicity of  $1/4$  ( $1/2$ ) in moiré filling. (e-g)  $\nu_{tTLG} - D$  map of  $R_{xx}$  (top panel),  $R_{xx}$  (middle panel) and Hall density  $n_{Hall}$  (bottom panel) as a function of  $\nu_{tTLG}$  in the moiré filling range of (e)  $-1 < \nu_{tTLG} < 1$ , (f)  $2 < \nu_{tTLG} < 4 + \frac{1}{4}$ , and (g)  $3.5 < \nu_{tTLG} < 8.5$ . (d) Schematics of the spatial charge distribution of DW states with periodicity of  $1/2$  (top panel) and  $1/4$  (bottom two panels) in moiré filling.

of  $\theta = 1.25^\circ$ ,  $1.35^\circ$  and  $1.5^\circ$ , respectively. In all samples, tTLG and the hBN substrate are maximally misaligned to minimize the influence of the hexagonal boron nitride (hBN) substrate (see Fig. S11) [28]. Also the angle between tTLG and WSe<sub>2</sub> is large such that the main effect of the latter is to induce effective, translation invariant, spin-orbit coupling terms in the graphene sheet closest to

WSe<sub>2</sub> [see Eq. (S11), SI 1]. We will focus our discussion on the transport behavior of sample A, while comparing all three samples in the supplemental section [28].

First we examine the transport behavior of sample A in the  $\nu_{tTLG} - D$  plane. Longitudinal resistance  $R_{xx}$  exhibits a series of resistance peaks emerging from partial band filling (Fig. 1b), indicative of correlation-driven insula-

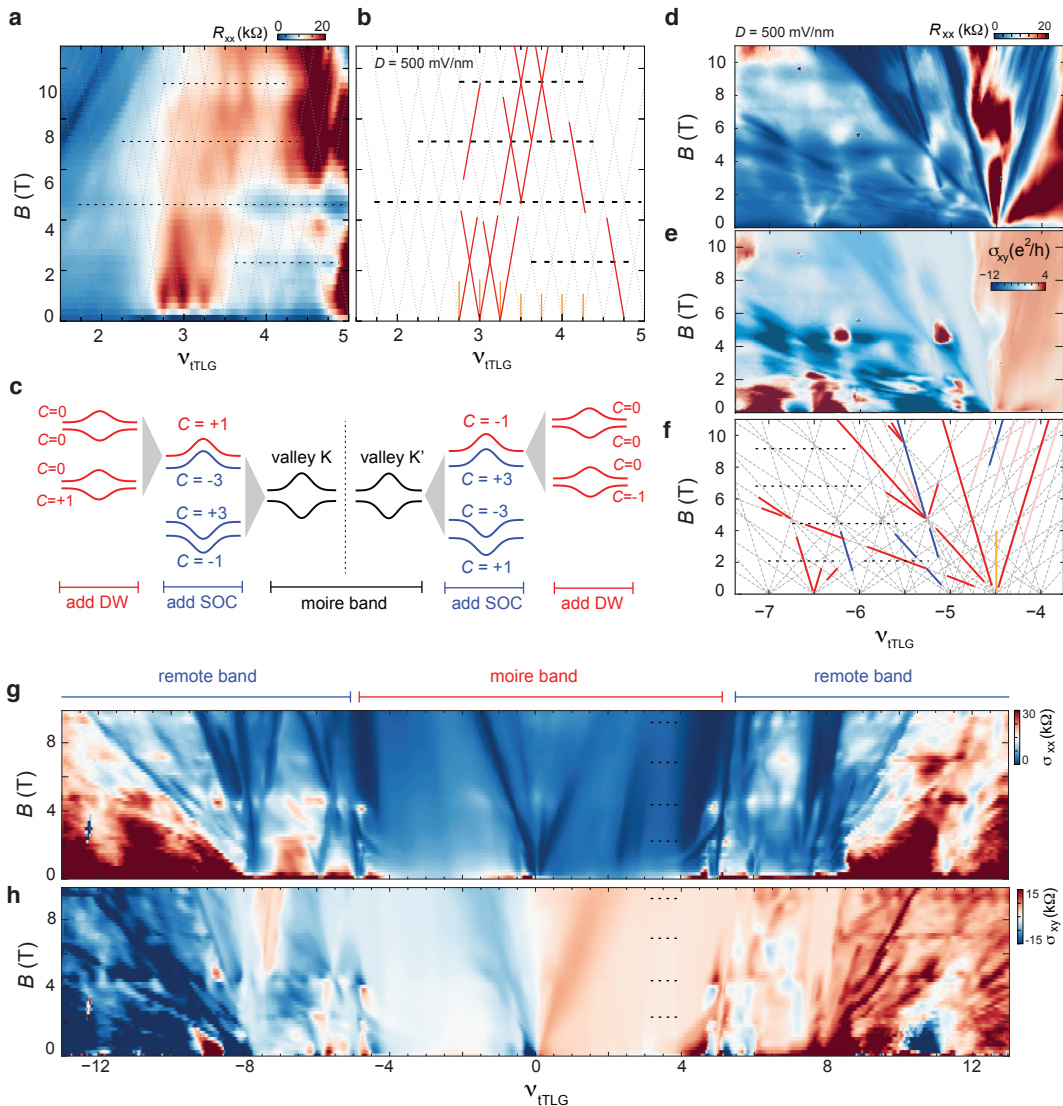


FIG. 2. **Incompressible states with a perpendicular magnetic field.** (a)  $\nu_{tTLG} - B$  map of  $R_{xx}$  around half-filled moiré band measured at  $D = 500$  mV/nm. (b) Schematic summarizing the most prominent features in panel (a). Red solid lines highlights broken symmetry Chern insulators (SBCI) with half-integer intercept. Yellow vertical lines correspond to DW states. Horizontal dashed lines mark every half magnetic flux per two moiré cell. (c) Schematic illustration of the evolution of the moiré bands in the tBLG sector of tTLG with SOC and  $1/4$  DW order. The indicated Chern numbers  $C$  are for illustration purposes (see main text) and represent just one of many possible scenarios.  $\nu_{tTLG} - B$  map of (d)  $R_{xx}$  and (e)  $\sigma_{xy}$  in the remote band measured at  $D = 500$  mV/nm and  $T = 20$  mK. (f) Schematics of the main features in (d) and (e). Apart from the SBCI with half-integer intercept (red solid lines) and DW states (yellow solid lines), pink solid lines indicate SBCI with  $1/8$  intercept. (g) Longitudinal conductance  $\sigma_{xx}$  and (h) Hall conductance  $\sigma_{xy}$  as a function of  $\nu_{tTLG}$  and  $B$ , measured at  $D = -300$  mV/nm and  $T = 1$  K. The horizontal dashed lines correspond to high-symmetry points in the Hofstadter spectrum.

tors. The positions of the most pronounced correlated insulators are labeled in the schematic  $\nu_{tTLG} - D$  phase diagram in Fig. 1c. In order to determine the filling fraction of the moiré band, we calculate moiré filling and displacement field based on the voltage bias applied onto the top and bottom gate electrodes using a simple capacitance model without fitting parameter. The only inputs are the position of the charge neutrality point (CNP) and moiré band gap: we assign the CNP as  $\nu_{tTLG} = 0$ , and a com-

pletely filled (empty) moiré band as  $\nu_{tTLG} = +4$  ( $-4$ ) (see Supplemental Fig. S2 and Fig. S3) [28]. Remarkably, all resistance peaks in the  $\nu_{tTLG} - D$  phase diagram, across both the flat and remote energy bands, match integer multiples of  $1/2$  or  $1/4$  moiré fillings. The abundance of correlated insulators at fractional moiré filling points towards density wave (DW) instabilities [29, 30] that break the moiré translation symmetry spontaneously, driven by long-range Coulomb correlations on a length scale longer

than one moiré wavelength. In the following, we will refer to these DW states according to the periodicity of their emergence as a function of  $\nu_{tTLG}$ . For example, the blue and red solid lines in Fig. 1c represent 1/4 and 1/2 DW states, respectively; the associated spatial modulation of their order parameter is illustrated on the triangular lattice in Fig. 1d. The nematicity in the spatial modulation can be detected through transport anisotropy defined as  $R_{xy}/R_{xx}$ . Strong anisotropy is observed in the portion of the phase space occupied by the 1/2 DW states, whereas no clear anisotropy is associated with 1/4 DW states (see Supplemental Fig. S10). This suggests that spatial modulation of the 1/4 DW state likely adopts the non-nematic option as shown on the left hand side of Fig. 1d. Note that the transport features we observe, e.g., in Fig. 1b, are manifestly not symmetric under  $D \rightarrow -D$  at fixed  $\nu_{tTLG}$ , while approximately invariant under simultaneous sign change of  $D$  and  $\nu_{tTLG}$ . The former asymmetry is a direct demonstration of the proximity effect of the WSe<sub>2</sub> crystal which, by virtue of only being present on one side, breaks the mirror symmetry of tTLG; the approximate symmetry under  $(D, \nu_{tTLG}) \rightarrow (-D, -\nu_{tTLG})$  is consistent with our band-structure calculations that also lead to density of states that are approximately invariant under this transformation, see Fig. S1b and c [28].

It is important to point out that we do not observe a clear hierarchy between correlated insulators at integer and fractional fillings, which has been a ubiquitous signature of TI-FSB in moiré systems. No indications of correlated insulators at fractional fillings in tTLG without proximity effect have been reported so far. Meanwhile, in twisted bilayers of graphene and TMD [29–31], correlation-driven states at fractional fillings are found to be much weaker compared to those at integer filling. This contrasting behavior offers a strong indication that the proximity effect of WSe<sub>2</sub> significantly alters the energetics of correlation-driven phenomena in tTLG and reveals DW phases as an integral flavor of moiré physics.

As expected theoretically, the emergence of 1/4 (1/2) DW order leads to a complex reconstruction of the moiré bands into 4 (2) sub bands each, splitting the van Hove singularity (vHs) of the unreconstructed bandstructure into multiple peaks (see SI 2 and Fig. S1d [28] for a demonstration). This is expected to induce complex signatures in the  $\nu_{tTLG}$ -dependence of  $n_{Hall}$ , which we indeed observe: at  $\nu_{tTLG} = \pm 1/2$ , resistance peaks are accompanied by resets in Hall density, where  $n_{Hall}$  diminishes at the onset of DW order (Fig. 1e). The fact that the density of mobile charge carriers is suddenly reduced is indicative of, at least, a partial gap opening in the Brillouin zone due to DW order. At higher densities, we also observe multiple vHs-like features in  $n_{Hall}$  with diverging density of states (Fig. 1f-g). A more direct demonstration of the DW-induced band reconstruction is provided by the behavior of incompressible states

in the presence of a perpendicular magnetic field. It is well established that an emerging Fermi surface will give rise to a Landau fan in the quantum Hall effect regime. In the density range of  $1 < \nu_{tTLG} < 4$ , where 1/4 DW dominates in the low-field limit, the fan diagram shown in Fig. 2a-b reveals a series of incompressible states that emanate from the 1/4 DW states. The emergence of Landau fans at density interval of 1/4 moiré filling suggests that a new sub band is associated with each DW state.

The linearly-dispersing incompressible states in the quantum Hall effect regime can be classified by a pair of quantum numbers  $(t, s)$  from the Diophantine equation  $\nu = t\phi/\phi_0 + s$ , where  $\nu$  is the filling factor  $\nu_{tTLG}$  at the incompressible state,  $\phi$  is the magnetic flux per moiré unit cell, and  $\phi_0$  is the magnetic flux quantum [30, 32]. Here  $s$  is the intercept of each incompressible state and the slope  $t$  is equal to its Chern number,  $C = t$ , according to the Streda formula [33]. We can see in Fig. 2a-b that there are multiple symmetry-broken Chern insulators (SBCI), characterized by fractional intercept  $s$  and integer  $C \neq 0$ ; these are likely to emerge via a  $B$ -induced first order phase transition [34] out of the DW states that are only present at low magnetic fields. To illustrate this further in a simple toy model, let us focus on the twisted-bilayer-graphene-like bands (see SI 1 [28]) of tTLG which can be split into Chern bands by the proximity-induced SOC [18], as shown schematically in Fig. 2c. The DW order in the range  $3 < \nu_{tTLG} < 4$  can now be viewed as splitting the topmost band in each valley into 4 subbands that are sequentially filled (zero Chern number for all fillings can be ensured by coherently occupying two DW bands with opposite valley indices, see SI 2 [28]). For sufficiently large  $B$ , states with non-zero Chern number, e.g., by occupying different combinations of the subbands arising from the  $|C| = 1, 3$  bands in Fig. 2c, are expected to be favored.

Many additional SBCI states are observed in the remote band (Fig. 2d-f). The quantized Hall resistance plateau and vanishing  $R_{xx}$  indicates that these incompressible states are fully developed, especially at large  $B$  (see Supplemental Fig. S9). At  $B < 4$  T,  $s$  takes predominantly half integer values, which is consistent with the 1/2 DW in the low field limit. Upon increasing  $B$  above 4T, we observe a series of BCSI states with 1/4 and 1/8 intercept, which are marked with pink solid lines in Fig. 2f. It is important to note that, for all incompressible states in the remote band,  $t$  takes on values of  $\pm 2, \pm 6, \pm 10 \dots$  (Supplemental Fig. S14), which yields important constraints on the underlying reconstructed band structure.

Notably, Fig. 2g-h reveal a series of prominent horizontal features over the density range of the flat and remote energy bands, with magnetic field values indicated by horizontal dashed lines. Along these features, longitudinal conductance exhibits a maximum and Hall conductance reverses sign. These behaviors are indica-

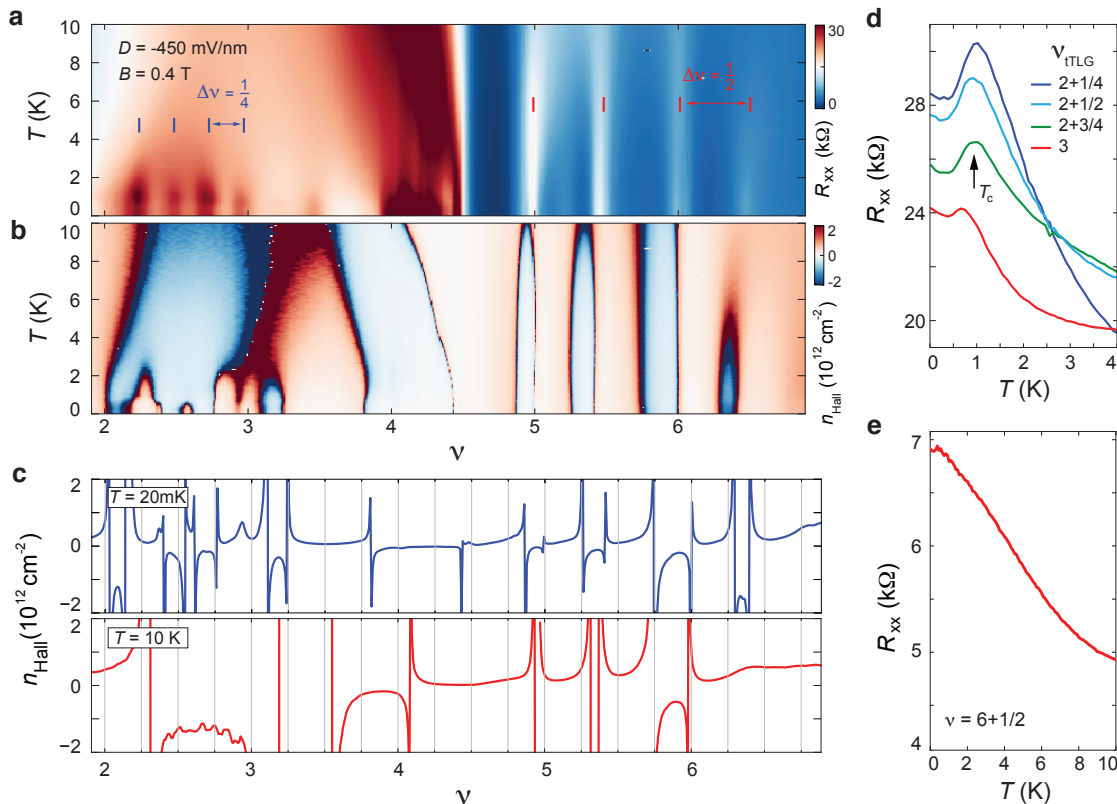


FIG. 3. **The temperature dependence of DW states.** (a) Longitudinal resistance  $R_{xx}$  and (b) Hall density  $n_{Hall}$  as a function of  $\nu_{tTLG}$  and temperature  $T$  measured at  $D = -450$  mV/nm and  $B = 0.4$  T. (c)  $n_{Hall}$  as a function of  $\nu_{tTLG}$  measured at  $T = 20$  mK (upper panel) and 10 K (lower panel). (d-e)  $R_{xx}$  as a function of temperature measured at (d)  $1/4$  and (e)  $1/2$  DW states. The measurement is performed with  $B = 0.4$  T.

tive of a high symmetry point in the recursive structure of the Hofstadter butterfly spectrum [35–37]. The most pronounced horizontal feature at  $B \sim 5$  T corresponds to one magnetic flux every four moiré unit cell,  $4\phi/\phi_0 = 0.5$ , which is in excellent agreement with the periodicity of the DW states [DW bands have one charge carrier for every four moiré unit cells, see Fig. 1d and Fig. S3] [28]. As such, four moiré wavelengths appears to be a special length scale for correlation-driven ground state order. It is also worth mentioning that the observation of these high symmetry points in the  $B$ - $\nu_{tTLG}$  plane throughout the entire density range strongly indicates a well-defined moiré wavelength throughout the sample, confirming that the twist angle is uniform.

The DW states exhibit a melting transition with increasing temperature, which is evidenced by the non-monotonic temperature dependence in  $R_{xx}$  (Fig. 3a). The melting temperature  $T_c$  is defined as the temperature where  $R_{xx}$  is maximal. For DW states in the density range of  $2 < \nu_{tTLG} < 4$ ,  $T_c$  is shown to be  $\sim 1$  K (Fig. 3d). At this temperature, the vHSs also disappear (Fig. 3b and c), providing further confirmation that the DW instability is Coulomb driven. Most importantly, the

lack of hierarchy is further demonstrated by the melting temperature, which is similar between integer and fractional fillings (Fig. 3d). Additionally, we note that a melting temperature of  $\sim 1$  K is much weaker compared to the correlated insulators at integer filling of graphene moiré systems without proximity effect, which typically has an energy gap of 10 – 30 K [3, 4].

Having discussed the main phenomenology associated with the abundance of insulating states at various fractional fillings, we are now in position to address possible relations to twist angle mismatch between top/middle and middle/bottom graphene layers in our tTLG sample. While a reconstruction of the moiré bands could theoretically be induced by a moiré pattern of moiré unit cells, resulting from a fine-tuned twist-angle mismatch [38], we believe that this scenario provides a much less natural interpretation of our findings than an interaction-induced DW instability. First, unlike moiré-induced band reconstruction which will give rise to an approximately temperature independent gap, the vHSs associated with  $1/4$  DW states disappear with increasing temperature at  $T \sim 1$  K (Supplemental Fig. 3) [28]. This points towards a Coulomb-driven origin. Second, in a separate work [39],

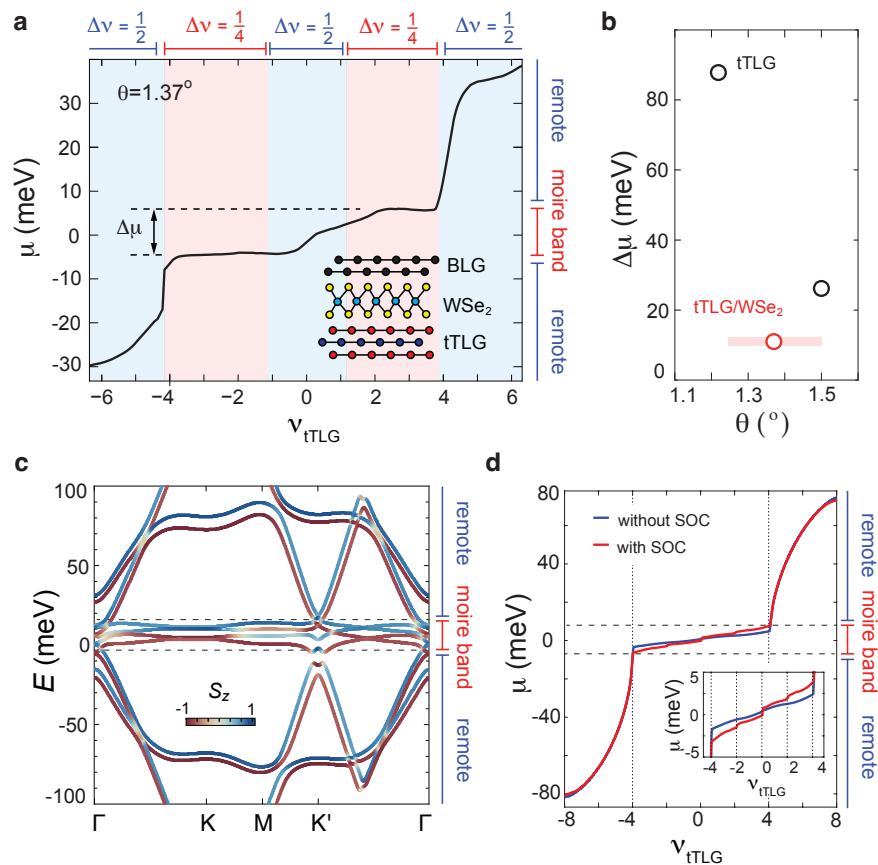


FIG. 4. **The influence of proximity effect on the band structure of tTLG.** (a) Chemical potential  $\mu$  measured in sample B, with twist angle of  $1.35^\circ$ , as a function of moiré filling  $\nu_{tTLG}$ . (b) Moiré band width extracted from chemical potential of tTLG samples with different twist angle  $\theta$ . Black open circles denote bandwidth measured from tTLG without proximity effect. Red open circle marks the bandwidth measured from sample B (tTLG/WSe<sub>2</sub> heterostructure). The red shaded bar denote the twist angle range where correlated insulators are observed in transport measurements, which provides strong indication of a flat energy band. (c) Calculated band structure of tTLG in proximity with WSe<sub>2</sub>, see SI 1 [28] for details. (d) Dependence of the chemical potential  $\mu$  on moiré filling  $\nu_{tTLG}$  resulting from the band structure in (c).

we show that superconductivity is stabilized in this sample at  $B = 0$ . If twist angle mismatch gave rise to a 4-fold enlarged moiré supercell, superconductivity would be expected to exhibit a density modulation with 1/4 filling periodicity. However, despite the emergence of superconductivity in regions of the  $\nu_{tTLG}$ - $D$  phase diagram where DW states are present at small magnetic fields, its robustness is largely insensitive to the density modulation. Finally, a density modulation of 1/2 and 1/4 filling has been observed in three separate samples with twist angles spanning a range of  $1.25^\circ$  to  $1.5^\circ$  degrees [28]. An accidental twist angle mismatch is unlikely to yield such reproducibility. This is further supported by the following observations: (i) the location of all correlated insulators throughout the density range is accurately matched with integer multiple of 1/2 and 1/4 without any fitting parameter; (ii) a high symmetry point in the Hofstadter spectrum is observed at  $\phi/\phi_0 = 1/4$  over the full density range. These observations highlights a well-defined moiré wavelength and excellent homogeneity of the tTLG sam-

ple, whereas a twist angle mismatch is known to give rise to sample inhomogeneity [38]. Combined, our findings suggest that the insulating phases at fractional fillings are correlation-driven DW instabilities, which are intrinsic to the tTLG/WSe<sub>2</sub> heterostructure, rather than a result of twist-angle mismatch.

To better understand the band structure of the tTLG/WSe<sub>2</sub> heterostructure and its connection to DW instabilities, we will directly probe the bandwidth of tTLG using the double-layer geometry shown in the inset of Fig. 4a. In sample B, Bernal bilayer graphene (BLG) is separated from tTLG by a crystal of WSe<sub>2</sub> with a thickness of 5 nm. The location of the CNP in BLG directly reflects the screening of electric field from the bottom gate electrode, which allows us to extract the chemical potential of tTLG,  $\mu_{tTLG}$ , as a function of  $\nu_{tTLG}$ . As can be seen in Fig. 4a,  $\mu_{tTLG}$  jumps abruptly at  $\nu_{tTLG} = \pm 4$ , which corresponds to the energy gap between the flat and remote bands [40, 41]. The bandwidth of the flat band, defined by the net increase of  $\mu_{tTLG}$  across the moiré

band, is less than 10 meV (Fig. 4b). This measured bandwidth is much smaller compared to bandwidth values measured from tBLG (40 meV-60 meV) [11, 40] and tTLG ( $\sim 30$  meV) [41]. In fact, very flat low-energy moiré bands were observed at  $1.25^\circ$  (sample A),  $1.35^\circ$  (sample B) and  $1.50^\circ$  (sample C), evidenced by the observation of correlated insulating states at partial filling. It is important to note that the measured bandwidth of tTLG, in the absence of proximity effect from WSe<sub>2</sub>, increases rapidly when the twist angle deviates from the magic angle of  $1.55^\circ$  [42], see Fig. 4b. As such, the small bandwidth in the tTLG/WSe<sub>2</sub> heterostructure at a twist angle far detuned from the magic angle sheds new light into the influence of the proximity effect from the tTLG/WSe<sub>2</sub> interface.

The key parameters determining the twist-angle  $\theta$  dependence of the bandwidth in a continuum model description [43] of twisted graphene systems are the intra- ( $w_0$ ) and inter-sublattice ( $w_1$ ) tunneling strengths. For  $w_0 = w_1 = w$ , one finds a sharp minimum of the bandwidth as a function of  $\theta$ , consistent with the behavior in Fig. 4b for tTLG without WSe<sub>2</sub>. While reducing  $w$  from the frequently used value  $w = 110$  meV could potentially explain the flat-band behavior of the three samples, we notice that  $w_0 = 0.875w$ ,  $w_1 = w$ —encoding relaxation effects which, in turn, could be crucially affected by WSe<sub>2</sub>—leads to a drastic reduction of the bandwidth in a larger twist-angle range that includes  $\theta \sim 1.3^\circ$  and  $\theta \sim 1.5^\circ$ , as shown in Fig. S1a [28].

In Fig. 4d,  $\mu_{tTLG}$  is plotted as a function of  $\nu_{tTLG}$  calculated using the reduced ratio of  $w_0/w_1 = 0.875$  for  $\theta = 1.35^\circ$ . Adding SOC gives rise to an offset between bands with opposite spin polarizations (see Fig. 4c), which is manifested in extra steps in the otherwise smooth chemical potential in Fig. 4d. The excellent agreement between the model and measurement is intriguing. Given the flatness of the band dispersion, Coulomb interaction is expected to play a dominating role. However, the measured  $\mu_{tTLG}$  does not exhibit the telltale saw tooth pattern associated with flavor symmetry breaking [11–13, 44]. At the same time, the energy dependence of the density of states of the moiré bands, encoded in the measured  $\mu = \mu(\nu_{tTLG})$ , further supports the connection between Coulomb correlations and DW order: in the density range near half filled moiré band, which is marked by the red shaded background in Fig. 4a,  $\mu_{tTLG}$  is almost a constant as a function of  $\nu_{tTLG}$ , demonstrating an extremely flat dispersion and high density of states. This density range is predominantly occupied by DW states with  $1/4$  periodicity. On the other hand, the band dispersion is more prominent near the CNP and the remote band (blue shaded background in Fig. 4a), where DW states appear with density interval of  $1/2$  moiré filling (Fig. 1e and g). Combined, these observations suggest that stronger Coulomb correlation induces more DW instabilities within a fixed window of carrier density.

It is worth pointing out the distinctions between the tTLG/WSe<sub>2</sub> heterostructure and moiré systems where DW and SBCI are previously observed [29, 30]. In twisted bilayer of TMD and magic-angle graphene moiré structures, correlated insulators at integer fillings are more robust compared to those appearing at fractional filling. In addition, most DW and SBCI in these systems are parameterized by  $s = N/3$  or  $N/5$ , where  $N$  takes integer values. On the other hand, correlation driven insulators in the tTLG/WSe<sub>2</sub> heterostructure exhibits density modulation of  $1/2$ ,  $1/4$  and  $1/8$  moiré filling. At the same time, there is no observable hierarchy between integer and fractional fillings. These findings suggest that long range Coulomb correlation plays a dominating role in the presence of proximity effect. Although it is unclear why moiré filling of  $1/2$  and  $1/4$  are more stable compared to  $1/3$  or  $1/5$ , we anticipate that our results will motivate future experimental and theoretical efforts to examine the mechanism underlying the DW instability in graphene moiré structures and the influence of the graphene/TMD interface. Establishing the role of DW instabilities in the phase diagram of twisted graphene systems adds a new flavor of physics that is ubiquitous to the cuprate materials. This could prove crucial in understanding fundamental connections and differences between these strongly correlated materials. At the same time, it unlocks an interesting test ground to investigate the relation between DW instabilities and the superconducting phase in tTLG on WSe<sub>2</sub>, which is discussed in Ref. [39].

## ACKNOWLEDGMENTS

This work was primarily supported by Brown University. Device fabrication was performed in the Institute for Molecular and Nanoscale Innovation at Brown University. The authors acknowledge the use of equipment funded by the MRI award DMR-1827453. H. D. Scammell acknowledges funding from ARC Centre of Excellence FLEET. K.W. and T.T. acknowledge support from the Elemental Strategy Initiative conducted by the MEXT, Japan (Grant Number JPMXP0112101001) and JSPS KAKENHI (Grant Numbers 19H05790, 20H00354 and 21H05233).

## COMPETING FINANCIAL INTERESTS

The authors declare no competing financial interests.

---

\* [jia.li@brown.edu](mailto:jia.li@brown.edu)

[1] E. Fradkin, S. A. Kivelson, and J. M. Tranquada, *Rev. Mod. Phys.* **87**, 457 (2015).

- [2] R. M. Fernandes, P. P. Orth, and J. Schmalian, *Annual Review of Condensed Matter Physics* **10**, 133 (2019).
- [3] Y. Cao, V. Fatemi, A. Demir, S. Fang, S. L. Tomarken, J. Y. Luo, J. D. Sanchez-Yamagishi, K. Watanabe, T. Taniguchi, E. Kaxiras, R. C. Ashoori, and P. Jarillo-Herrero, *Nature* **556**, 80 (2018).
- [4] Y. Cao, V. Fatemi, S. Fang, K. Watanabe, T. Taniguchi, E. Kaxiras, and P. Jarillo-Herrero, *Nature* **556**, 43 (2018).
- [5] X. Liu, Z. Hao, E. Khalaf, J. Y. Lee, Y. Ronen, H. Yoo, D. H. Najafabadi, K. Watanabe, T. Taniguchi, A. Vishwanath, *et al.*, *Nature* **583**, 221 (2020).
- [6] Y. Cao, D. Rodan-Legrain, O. Rubies-Bigorda, J. M. Park, K. Watanabe, T. Taniguchi, and P. Jarillo-Herrero, *Nature* **583**, 215 (2020).
- [7] S. Chen, M. He, Y.-H. Zhang, V. Hsieh, Z. Fei, K. Watanabe, T. Taniguchi, D. H. Cobden, X. Xu, C. R. Dean, and M. Yankowitz, *Nature Physics* **17**, 374 (2021).
- [8] H. Polshyn, J. Zhu, M. Kumar, Y. Zhang, F. Yang, C. Tschirhart, M. Serlin, K. Watanabe, T. Taniguchi, A. MacDonald, and A. F. Young, *Nature* **588**, 66 (2020).
- [9] J. M. Park, Y. Cao, K. Watanabe, T. Taniguchi, and P. Jarillo-Herrero, *Nature* **590**, 249 (2021).
- [10] Z. Hao, A. Zimmerman, P. Ledwith, E. Khalaf, D. H. Najafabadi, K. Watanabe, T. Taniguchi, A. Vishwanath, and P. Kim, *Science* **371**, 1133 (2021).
- [11] J. M. Park, Y. Cao, K. Watanabe, T. Taniguchi, and P. Jarillo-Herrero, *Nature* **592**, 43 (2021).
- [12] U. Zondiner, A. Rozen, D. Rodan-Legrain, Y. Cao, R. Queiroz, T. Taniguchi, K. Watanabe, Y. Oreg, F. von Oppen, A. Stern, *et al.*, *Nature* **582**, 203 (2020).
- [13] D. Wong, K. P. Nuckolls, M. Oh, B. Lian, Y. Xie, S. Jeon, K. Watanabe, T. Taniguchi, B. A. Bernevig, and A. Yazdani, *Nature* **582**, 198 (2020).
- [14] X. Lu, P. Stepanov, W. Yang, M. Xie, M. A. Aamir, I. Das, C. Urgell, K. Watanabe, T. Taniguchi, G. Zhang, A. Bachtold, A. H. MacDonald, and D. K. Efetov, *arXiv preprint arXiv:1903.06513* (2019).
- [15] M. Yankowitz, S. Chen, H. Polshyn, Y. Zhang, K. Watanabe, T. Taniguchi, D. Graf, A. F. Young, and C. R. Dean, *Science* **363**, 1059 (2019).
- [16] A. L. Sharpe, E. J. Fox, A. W. Barnard, J. Finney, K. Watanabe, T. Taniguchi, M. Kastner, and D. Goldhaber-Gordon, *arXiv preprint arXiv:1901.03520* (2019).
- [17] M. Serlin, C. Tschirhart, H. Polshyn, Y. Zhang, J. Zhu, K. Watanabe, T. Taniguchi, L. Balents, and A. Young, *arXiv preprint arXiv:1907.00261* (2019).
- [18] J.-X. Lin, Y.-H. Zhang, E. Morissette, Z. Wang, S. Liu, D. Rhodes, K. Watanabe, T. Taniguchi, J. Hone, and J. Li, *arXiv preprint arXiv:2102.06566* (2021).
- [19] H. S. Arora, R. Polski, Y. Zhang, A. Thomson, Y. Choi, H. Kim, Z. Lin, I. Z. Wilson, X. Xu, J.-H. Chu, *et al.*, *arXiv preprint arXiv:2002.03003* (2020).
- [20] M. Gmitra and J. Fabian, *Phys. Rev. B* **92**, 155403 (2015).
- [21] M. Gmitra and J. Fabian, *Phys. Rev. Lett.* **119**, 146401 (2017).
- [22] Z. Wang, D.-K. Ki, H. Chen, H. Berger, A. H. MacDonald, and A. F. Morpurgo, *Nature communications* **6**, 1 (2015).
- [23] Z. Wang, D.-K. Ki, J. Y. Khoo, D. Mauro, H. Berger, L. S. Levitov, and A. F. Morpurgo, *Phys. Rev. X* **6**, 041020 (2016).
- [24] B. Yang, M. Lohmann, D. Barroso, I. Liao, Z. Lin, Y. Liu, L. Bartels, K. Watanabe, T. Taniguchi, and J. Shi, *Physical Review B* **96**, 041409 (2017).
- [25] A. Avsar, J. Y. Tan, T. Taychatanapat, J. Balakrishnan, G. Koon, Y. Yeo, J. Lahiri, A. Carvalho, A. Rodin, E. O'Farrell, *et al.*, *Nature communications* **5**, 1 (2014).
- [26] J. Island, X. Cui, C. Lewandowski, J. Khoo, E. Spanton, H. Zhou, D. Rhodes, J. Hone, T. Taniguchi, K. Watanabe, L. Levitov, M. Zaletel, and A. Young, *Nature* , 1 (2019).
- [27] T. Wang, N. Bultinck, and M. P. Zaletel, *Physical Review B* **102**, 235146 (2020).
- [28] Please see the supplementary materials.
- [29] Y. Xu, S. Liu, D. A. Rhodes, K. Watanabe, T. Taniguchi, J. Hone, V. Elser, K. F. Mak, and J. Shan, *Nature* **587**, 214 (2020).
- [30] Y. Xie, A. T. Pierce, J. M. Park, D. E. Parker, E. Khalaf, P. Ledwith, Y. Cao, S. H. Lee, S. Chen, P. R. Forrester, *et al.*, *arXiv preprint arXiv:2107.10854* (2021).
- [31] A. T. Pierce, Y. Xie, J. M. Park, E. Khalaf, S. H. Lee, Y. Cao, D. E. Parker, P. R. Forrester, S. Chen, K. Watanabe, *et al.*, *arXiv preprint arXiv:2101.04123* (2021).
- [32] E. M. Spanton, A. A. Zibrov, H. Zhou, T. Taniguchi, K. Watanabe, M. P. Zaletel, and A. F. Young, *Science* **360**, 62 (2018).
- [33] P. Streda, *Journal of Physics C: Solid State Physics* **15**, L717 (1982).
- [34] B. Lian, Z.-D. Song, N. Regnault, D. K. Efetov, A. Yazdani, and B. A. Bernevig, *Phys. Rev. B* **103**, 205414 (2021).
- [35] C. R. Dean, L. Wang, P. Maher, C. Forsythe, F. Ghahari, Y. Gao, J. Katoch, M. Ishigami, P. Moon, M. Koshino, *et al.*, *Nature* **497**, 598 (2013).
- [36] B. Hunt, J. D. Sanchez-Yamagishi, A. F. Young, M. Yankowitz, B. J. LeRoy, K. Watanabe, T. Taniguchi, P. Moon, M. Koshino, P. Jarillo-Herrero, *et al.*, *Science* **340**, 1427 (2013).
- [37] L. Ponomarenko, R. Gorbachev, G. Yu, D. Elias, R. Jalil, A. Patel, A. Mishchenko, A. Mayorov, C. Woods, J. Wallbank, *et al.*, *Nature* **497**, 594 (2013).
- [38] S. Turkel, J. Swann, Z. Zhu, M. Christos, K. Watanabe, T. Taniguchi, S. Sachdev, M. S. Scheurer, E. Kaxiras, C. R. Dean, and A. N. Pasupathy, *arXiv:2109.12631* (2021).
- [39] P. Siriviboon, J.-X. Lin, H. D. Scammell, S. Liu, D. Rhodes, K. Watanabe, T. Taniguchi, J. Hone, M. S. Scheurer, and J. Li, *arXiv e-prints* (2021), [arXiv:xxxx.xxxx \[cond-mat.str-el\]](#).
- [40] Y. Saito, F. Yang, J. Ge, X. Liu, T. Taniguchi, K. Watanabe, J. Li, E. Berg, and A. F. Young, *Nature* **592**, 220 (2021).
- [41] X. Liu, K. Watanabe, T. Taniguchi, and J. Li, *arXiv preprint arXiv:2108.03338* (2021).
- [42] E. Khalaf, A. J. Kruchkov, G. Tarnopolsky, and A. Vishwanath, *Phys. Rev. B* **100**, 085109 (2019).
- [43] R. Bistritzer and A. H. MacDonald, *Proceedings of the National Academy of Sciences* **108**, 12233 (2011).
- [44] J. Kang, B. A. Bernevig, and O. Vafek, *arXiv preprint arXiv:2104.01145* (2021).
- [45] T. Naimier, K. Zollner, M. Gmitra, and J. Fabian, *arXiv e-prints* (2021), [arXiv:2108.06126 \[cond-mat.mes-hall\]](#).
- [46] M. Christos, S. Sachdev, and M. S. Scheurer, *arXiv preprint arXiv:2106.02063* (2021).

- [47] N. N. T. Nam and M. Koshino, *Phys. Rev. B* **96**, 075311 (2017).
- [48] S. Carr, S. Fang, Z. Zhu, and E. Kaxiras, *Phys. Rev. Research* **1**, 013001 (2019).
- [49] P. J. Ledwith, E. Khalaf, Z. Zhu, S. Carr, E. Kaxiras, and A. Vishwanath, arXiv e-prints (2021), [arXiv:2111.11060](https://arxiv.org/abs/2111.11060) [cond-mat.str-el].
- [50] Y. Saito, J. Ge, L. Rademaker, K. Watanabe, T. Taniguchi, D. A. Abanin, and A. F. Young, *Nature Physics* **17**, 478 (2021).
- [51] I. Das, X. Lu, J. Herzog-Arbeitman, Z.-D. Song, K. Watanabe, T. Taniguchi, B. A. Bernevig, and D. K. Efetov, *Nature Physics* **17**, 710 (2021).

## SUPPLEMENTARY MATERIALS

**Abundance of density wave phases in twisted trilayer graphene on  $\text{WSe}_2$** 

Phum Siriviboon, Jiang-Xiazi Lin, Harley D. Scammell, Song Liu, Daniel Rhodes, K. Watanabe, T. Taniguchi, James Hone, Mathias S. Scheurer, and J.I.A. Li<sup>†</sup>

<sup>†</sup> Corresponding author. Email: jia.li@brown.edu

**This PDF file includes:**

Supplementary Text  
Materials and Methods  
Figs. S1 to S19  
References (44-47)

### SI 1: Bandstructure calculations

**Noninteracting model.** Here we will state the detailed form of the non-interacting Hamiltonian we use for twisted trilayer graphene in proximity to a WSe<sub>2</sub> layer. We describe the non-interacting bands of the trilayer graphene system within a continuum model; using an extension of the Bistritzer-MacDonald (BM) model [43] which accounts for the three layers.

To define the Hamiltonian, let  $c_{\mathbf{k};\rho,l,\eta,s,\mathbf{G}}$  denote the operator annihilating an electron at crystalline momentum  $\mathbf{k}$  in the moiré Brillouin zone (MBZ), of spin  $s = \uparrow, \downarrow$ , in sublattice  $\rho = A, B$  and valley  $\eta = \pm$  of the microscopic graphene sheets, within layer  $l = 1, 2, 3$ , and with reciprocal lattice (RL) vector  $\mathbf{G} = \sum_{j=1,2} n_j \mathbf{G}_j$ ,  $n_j \in \mathbb{Z}$  of the moiré lattice. We will use the same symbol with subscript  $j = 0, 1, 2, 3$  for Pauli matrices and the associated quantum numbers.

It is convenient [42] to perform a unitary transformation in layer space,

$$c_{\mathbf{k};\rho,l,\eta,s,\mathbf{G}} = V_{l,\ell} \psi_{\mathbf{k};\rho,\ell,\eta,s,\mathbf{G}}, \quad V = \frac{1}{\sqrt{2}} \begin{pmatrix} 1 & 0 & -1 \\ 0 & \sqrt{2} & 0 \\ 1 & 0 & 1 \end{pmatrix} \quad (\text{S1})$$

that decomposes the system into mirror-even,  $\ell = 1, 2$ , and mirror-odd,  $\ell = 3$ , subspaces. Without spin-orbit coupling (SOC) and displacement field, these subspaces will be decoupled as follows from mirror symmetry and can be seen explicitly below. After this transformation, the continuum model is

$$H_0^{\text{Full}} = \sum_{\mathbf{k} \in \text{MBZ}} \sum_{\rho, \rho' = A, B} \sum_{\ell, \ell' = 1, 2, 3} \sum_{\eta = \pm} \sum_{s = \uparrow, \downarrow} \sum_{\mathbf{G}, \mathbf{G}' \in \text{RL}} \psi_{\mathbf{k};\rho,\ell,\eta,s,\mathbf{G}}^\dagger (h_{\mathbf{k},\eta})_{\rho,\ell,\mathbf{G};\rho',\ell',\mathbf{G}'} \psi_{\mathbf{k};\rho',\ell',\eta,s,\mathbf{G}'}, \quad (\text{S2})$$

where

$$h_{\mathbf{k},\eta} = h_{\mathbf{k},\eta}^{(g)} + h_{\mathbf{k},\eta}^{(t)} + h_{\mathbf{k}}^{(D)} + h_{\mathbf{k},\eta}^{(\text{SOC})}. \quad (\text{S3})$$

Here the contributions are: graphene kinetic terms  $h_{\mathbf{k},\eta}^{(g)}$ , interlayer tunnelling  $h_{\mathbf{k},\eta}^{(t)}$ , displacement field  $h_{\mathbf{k}}^{(D)}$ , and proximity-induced SOC  $h_{\mathbf{k},\eta}^{(\text{SOC})}$  due to the WSe<sub>2</sub> layer.

In the mirror basis, the decoupled graphene kinetic terms are

$$\left( h_{\mathbf{k},+}^{(g)} \right)_{\rho,\ell,\mathbf{G};\rho',\ell',\mathbf{G}'} = \delta_{\ell,\ell'} \delta_{\mathbf{G},\mathbf{G}'} v_F (\boldsymbol{\rho}_{\theta_\ell})_{\rho,\rho'} (\mathbf{k} + \mathbf{G} - (-1)^\ell \mathbf{q}_1/2), \quad (\text{S4})$$

$$\left( h_{\mathbf{k},-}^{(g)} \right)_{\rho,\ell,\mathbf{G};\rho',\ell',\mathbf{G}'} = \left( h_{-\mathbf{k},+}^{(g)} \right)_{\rho,\ell,-\mathbf{G};\rho',\ell',-\mathbf{G}'}, \quad (\text{S5})$$

where  $\boldsymbol{\rho}_\theta = e^{i\theta\rho_3/2} \boldsymbol{\rho} e^{-i\theta\rho_3/2}$ , and  $\mathbf{q}_1$  connecting the K and K' points in the MBZ. Moreover, in this basis, the Hamiltonian

$$\left( h_{\mathbf{k},+}^{(t)} \right)_{\rho,\ell,\mathbf{G};\rho',\ell',\mathbf{G}'} = \sqrt{2} \begin{pmatrix} 0 & (T_{\mathbf{G}-\mathbf{G}'}_{\rho,\rho'}) & 0 \\ (T_{\mathbf{G}'-\mathbf{G}}^*_{\rho',\rho}) & 0 & 0 \\ 0 & 0 & 0 \end{pmatrix}_{\ell,\ell'}, \quad (\text{S6})$$

$$\left( h_{\mathbf{k},-}^{(t)} \right)_{\rho,\ell,\mathbf{G};\rho',\ell',\mathbf{G}'} = \left( h_{-\mathbf{k},+}^{(t)} \right)_{\rho,\ell,-\mathbf{G};\rho',\ell',-\mathbf{G}'}, \quad (\text{S7})$$

which accounts for the tunnelling modulated on the moiré lattice, only couples the mirror-odd sectors, as required by symmetry. Here we use the BM form,

$$T_{\delta\mathbf{G}} = \sum_{j=-1,0,1} \delta_{\delta\mathbf{G}+\mathbf{A}_j,0} \left[ w_0 \rho_0 + w_1 \begin{pmatrix} 0 & \omega^j \\ \omega^{-j} & 0 \end{pmatrix} \right], \quad (\text{S8})$$

$$\omega = e^{i\frac{2\pi}{3}}, \quad \mathbf{A}_0 = 0, \quad \mathbf{A}_1 = \mathbf{G}_1, \quad \mathbf{A}_2 = \mathbf{G}_1 + \mathbf{G}_2. \quad (\text{S9})$$

Note that  $T_{\delta\mathbf{G}}^\dagger = T_{\delta\mathbf{G}}$  and  $\rho_x T_{\delta\mathbf{G}} \rho_x = T_{\delta\mathbf{G}}^*$ . Furthermore, the term induced by the displacement field,  $D$ , is given by

$$\left( h_{\mathbf{k}}^{(D)} \right)_{\rho,\ell,\mathbf{G};\rho',\ell',\mathbf{G}'} = -D \delta_{\rho,\rho'} \delta_{\mathbf{G},\mathbf{G}'} \begin{pmatrix} 0 & 0 & 1 \\ 0 & 0 & 0 \\ 1 & 0 & 0 \end{pmatrix}_{\ell,\ell'}, \quad (\text{S10})$$

which breaks the mirror symmetry, and therefore couples the different mirror-eigenvalue sectors.

The final ingredient is the proximity-induced SOC. We account for induced SOC only in the graphene layer,  $l = 1$ , which is nearest to the WSe<sub>2</sub>, i.e., the top layer in Fig. 1a. Making use of the known [20, 45] form of the proximity-induced SOC in a single graphene layer, we arrive at

$$H^{\text{SOC}} = \sum_{\mathbf{k} \in \text{MBZ}} \sum_{\rho, \rho' = A, B} \sum_{\eta = \pm} \sum_{s, s' = \uparrow, \downarrow} \sum_{\mathbf{G} \in \text{RL}} c_{\mathbf{k}; \rho, 1, \eta, s, \mathbf{G}}^\dagger (h_\eta^{\text{SOC}, l=1})_{\rho, s; \rho', s'} c_{\mathbf{k}; \rho', 1, \eta, s', \mathbf{G}}, \quad (\text{S11a})$$

$$h_\eta^{\text{SOC}, l=1} = \lambda_I s_z \eta + \lambda_R (\eta \rho_x s_y - \rho_y s_x) + \lambda_{\text{KM}} \eta \rho_z s_z + m \rho_z. \quad (\text{S11b})$$

The four terms describe Ising  $\lambda_I$ , Rashba  $\lambda_R$ , and a ‘‘Kane-Mele’’  $\lambda_{\text{KM}}$  types of SOC. We also include a mass term  $m$ , which accounts for  $C_{2z}$  breaking due to the WSe<sub>2</sub> layer. Although the inclusion of  $m$  and  $\lambda_{\text{KM}}$  is computationally straightforward, we set  $m = \lambda_{\text{KM}} = 0$  in our explicit calculations below since these two SOC terms are expected to be negligible small for a significantly misaligned (cf. Fig. S11) WSe<sub>2</sub>-graphene heterostructure [45].

Upon transforming Eq. (S11) to the mirror eigenbasis according to Eq. (S1), we find

$$\left( h_{\mathbf{k}, \eta}^{(\text{SOC})} \right)_{\rho, \ell, \mathbf{G}; \rho', \ell', \mathbf{G}'} = \frac{\delta_{\mathbf{G}, \mathbf{G}'}}{2} \begin{pmatrix} (h_\eta^{\text{SOC}, l=1})_{\rho, \rho'} & 0 & (h_\eta^{\text{SOC}, l=1})_{\rho, \rho'} \\ 0 & 0 & 0 \\ (h_\eta^{\text{SOC}, l=1})_{\rho, \rho'} & 0 & (h_\eta^{\text{SOC}, l=1})_{\rho, \rho'} \end{pmatrix}. \quad (\text{S12})$$

The presence of WSe<sub>2</sub> on a single side breaks the mirror reflection symmetry explicitly, and therefore induces couplings between the mirror-even and mirror-odd sectors [off-diagonal terms in Eq. (S12)]. While we take these off-diagonal terms into account in our bandstructure calculations, we expect that their impact is subleading for generic momenta  $\mathbf{k}$  where the (approximately) mirror-even and mirror-odd bands for  $D = 0$  (at small  $D$ ) are energetically well-separated. In this limit, the main impact of the SOC coupling onto the mirror-even, ‘‘twisted-bilayer-graphene-like’’ [46], bands is the same as that of WSe<sub>2</sub> on twisted-bilayer graphene (modulo rescaling of parameters); the same holds for the mirror-even, ‘‘graphene-like’’, sector.

This completes our definition of all terms in the continuum-model Hamiltonian  $H_0^{\text{Full}}$  in Eq. (S2).

**Parameters and twist-angle dependence.** The noninteracting model (S2) predicts a magic angle near  $\theta \sim 1.55^\circ$ , for the standard set of parameters [43]:  $v_F/a = 2.7\sqrt{3}/2 \times 10^3$  meV,  $w_0 = w_1 = 110$  meV, and zero SOC. The resulting bandwidth for a twist angle of  $\theta \sim 1.37^\circ$  is much larger than what we observe experimentally for this angle [see Fig. 4b in the main text]. We have also checked that adding SOC does not change this conclusion.

To account for this difference within the noninteracting model, we allow for variations in the sublattice diagonal and off-diagonal interlayer hopping strengths,  $w_0$  and  $w_1$  respectively. This is motivated by the observation, in the absence of WSe<sub>2</sub> layer, that  $w_0 < w_1$  takes into account corrugation effects [47–49]. With this in mind, Fig. S1a shows the twist-angle dependence of the moiré bandwidth for two cases: (i)  $w_0 = 0.875w_1$ ,  $w_1 = w = 110$  meV, and (ii)  $w_0 = w_1 = 0.86w$ ,  $w = 110$  meV. A qualitative difference is seen; in case (i) there is a *magic dip* at  $\theta \approx 1.37^\circ$ , while for (ii) there is a direct shift of the *magic angle* down to  $\theta \approx 1.37^\circ$  (as expected since scaling the inter-layer coupling down is equivalent to decreasing the magic angle [43]). Further accounting for SOC on top of this broadens the bandwidth, and makes both cases consistent with the experimentally observed bandwidth of  $\sim 10$  meV, see Fig. 4c of the main text; in that plot, we used  $\lambda_I = \lambda_R = 10$  meV where  $\lambda_I = \lambda_R$  is motivated by the fact that these two SOC terms have been estimated [45] to be roughly the same for a relative of twist angle of  $\approx 20^\circ$  between graphene and WSe<sub>2</sub> see Fig. S11, and the absolute strength is chosen to approximately reproduce Fig. 4a of the main text. All results presented below and in the main text will take the inter-layer hopping parameters from case (i) and  $\lambda_I = \lambda_R = 10$  meV.

**Density of states.** Computing the density of states of the noninteracting Hamiltonian, taking  $w_0 = 0.875w_1$ ,  $w_1 = w = 110$  meV and  $\lambda_I = \lambda_R = 10$  meV, Figure S1(b) and (c) demonstrate two key features that are seen experimentally [namely Fig. 1(b) and (c) of the main text]: (i) the van Hove singularity (vHs) becomes more pronounced at finite  $D$ , although this enhancement is more subtle than seen experimentally, and (ii) that there is an asymmetry of  $D > 0$  and  $D < 0$  at fixed  $\nu$ , but approximate invariance under  $(D, \nu) \rightarrow (-D, -\nu)$ .

## SI 2: Density-wave order parameters

**Possible CDW order parameters.** Let us begin our theoretical discussion of possible DW phases with conventional charge density wave (CDW) order. By CDW we mean phases where moiré translational symmetry is broken by a spatial modulation of the electronic density while all flavor symmetries (in our case valley, but without SOC also

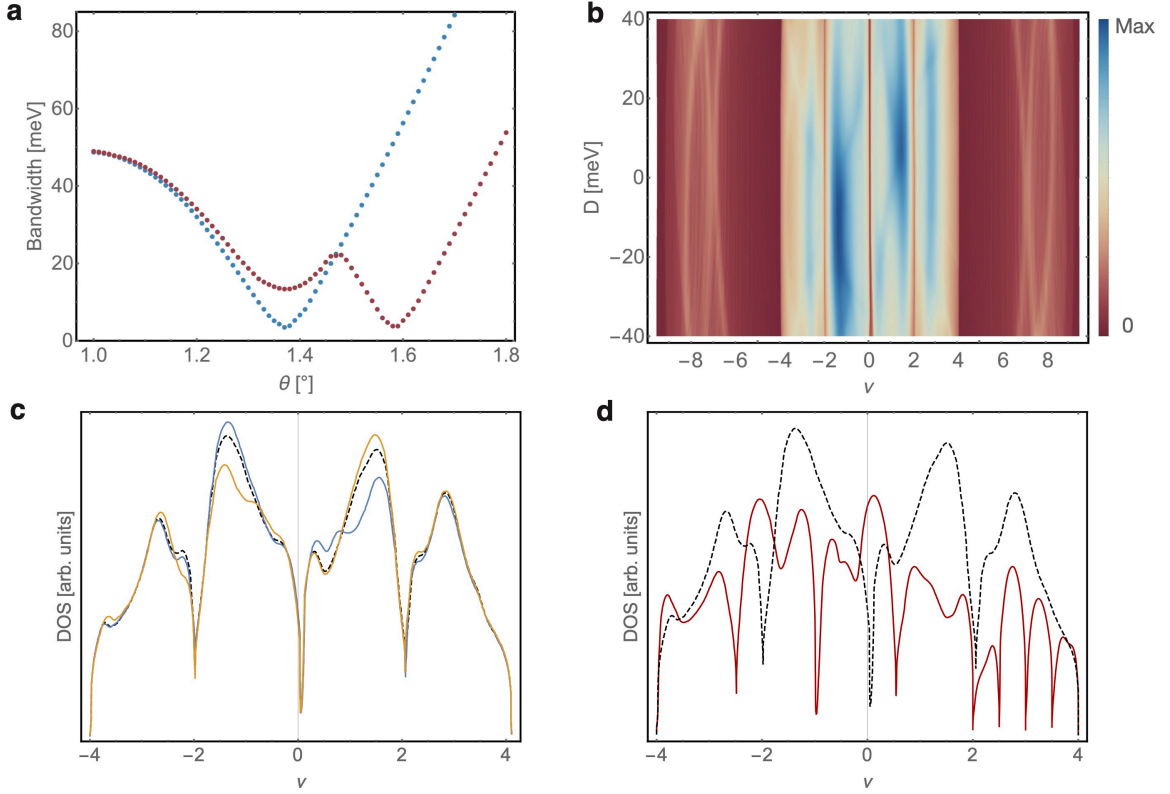


FIG. S1. (a) Bandwidth vs. twist angle, where blue and red points correspond to  $w_0 = w_1 = 0.86w$ ,  $w = 110$  meV and  $w_0 = 0.875w$ ,  $w_1 = w$ ,  $w = 110$  meV, respectively, and SOC is set to zero. Note the additional dip at  $\theta \approx 1.37^\circ$  for the red points. In (b), (c) and (d) we take  $w_0 = 0.875w$ ,  $w_1 = w$ ,  $w = 110$  meV, and  $\lambda_I = \lambda_R = 10$  meV. (b) Density of states as a function of  $\nu$  and  $D$ . (c) Black dashed, solid blue and solid orange correspond to  $D = \{0, 10, -10\}$  meV, respectively. An approximate symmetry  $(D, \nu) \rightarrow (-D, -\nu)$  is seen. Moreover, the van Hove peak becomes slightly more prominent for  $D = \pm 10$  meV relative to  $D = 0$ . (d) Red curve includes a DW order parameter  $\Phi_0 = 4\text{meV}$ , according to Eq. (S17), while the black dashed line is the reference density of states at  $\Phi_0 = 0$ .

spin) are preserved. Restricting the analysis to order parameters with momentum transfer given by any of the three M points of the MBZ,  $\mathbf{M}_j$ ,  $j = 1, 2, 3$ , the presence of CDW order can be described by a coupling of the form

$$H_\phi = \sum_{\mathbf{R} \in \text{ML}} \sum_{\eta, s, \alpha} \sum_{j=1}^3 \tilde{\phi}_j e^{i\mathbf{M}_j \mathbf{R}} c_{\mathbf{R}, \alpha, \eta, s}^\dagger c_{\mathbf{R}, \alpha, \eta, s} + \text{H.c.} = \sum_{\mathbf{R} \in \text{ML}} \sum_{\eta, s, \alpha} \sum_{j=1}^3 \phi_j \cos(\mathbf{M}_j \mathbf{R}) c_{\mathbf{R}, \alpha, \eta, s}^\dagger c_{\mathbf{R}, \alpha, \eta, s}. \quad (\text{S13})$$

Here  $c_{\mathbf{R}, \alpha, \eta, s}^\dagger$  creates an electron with spin  $s$ , in valley  $\eta$ , and in Wannier state  $\alpha$  in unit cell  $\mathbf{R}$  associated with a set of low-energy bands of interest. In the second equality, we used that  $e^{i\mathbf{M}_j \mathbf{R}} = e^{-i\mathbf{M}_j \mathbf{R}}$  allowing us to introduce the real-valued, three-component DW order parameter  $\phi_j = \tilde{\phi}_j + \tilde{\phi}_j^* \in \mathbb{R}$ .

Upon noting that the action of  $C_{3z}$  is  $\phi_j \rightarrow \phi_{(j+1 \bmod 3)}$  and that of an elementary translation by a primitive vector  $\mathbf{a}_{j'}$  is given by  $\phi_{j'} \rightarrow \phi_j$ ,  $\phi_{j \neq j'} \rightarrow -\phi_j$ , the free-energy up to quartic order in  $\phi_j$  can only have the form

$$\mathcal{F} \sim a(T) \sum_j \phi_j^2 + b \phi_1 \phi_2 \phi_3 + c_1 \left( \sum_j \phi_j^2 \right)^2 + c_2 [(\phi_1 \phi_2)^2 + (\phi_2 \phi_3)^2 + (\phi_3 \phi_1)^2], \quad (\text{S14})$$

where  $a$ ,  $b$ ,  $c_1$ , and  $c_2$  are real-valued, phenomenological parameters. To discuss the resulting phases, let us first consider  $b \rightarrow 0$ . It is easy to see that there are only two possible minima: if  $c_2 > 0$ , we find

$$\phi_1 = \Phi_0, \quad \phi_2 = \phi_3 = 0, \quad (\text{S15})$$

where  $\Phi_0 > 0$  without loss of generality, and symmetry-related configurations. This is the 2-unit-cell state in the upper panel of Fig. 1d. If  $c_2 < 0$ , we instead find

$$\phi_1 = \phi_2 = \phi_3 = -\text{sign}(b) \Phi_0, \quad \Phi_0 > 0, \quad (\text{S16})$$

as well as its symmetry-related states; this corresponds to the 4-unit-cell state shown in the lower panel, left part, of Fig. 1d. While finite values of  $b$  in Eq. (S14) do not lead to new phases as  $\phi_1\phi_2\phi_3$  is extremized if  $|\phi_1| = |\phi_2| = |\phi_3|$ ,  $b \neq 0$  has crucial consequences for the nature of the thermal phase transition: as is generically expected to be the case, let us assume that the temperature dependence of  $b$ ,  $c_1$ , and  $c_2$  can be neglected near the critical temperature  $T_c$ , where  $a(T)$  changes sign. We then see that, irrespective of the sign of  $c_2$ , the system will always first enter the 4-unit-cell state in Eq. (S16) right below  $T_c$ . If  $c_2 < 0$ , the system will stay in this phase at lower temperature [at least, as long as the expansion (S14) is valid]. However, in the case  $c_2 > 0$ , there will be a first order transition into the 2-unit-cell state at some temperature smaller than  $T_c$ . While these two temperatures can in principle be very close and, hence, might be hard to resolve, we do not see any sign of first-order transitions in the DW states, which provides further evidence in favor of the 4-unit-cell state in the lower left panel of Fig. 1d.

**Band reconstruction.** We next consider the influence of the 4-unit-cell CDW order, associated with the minimum in Eq. (S16), on the band structure. The corresponding impact on the moiré flat bands (i.e. the four bands, per valley  $\eta$ , in the vicinity of charge neutrality) is captured by the Hamiltonian,

$$H^{\text{DW}} = \sum_{\mathbf{k}} \sum_{\eta=\pm} \sum_{n=1}^4 \left( d_{\eta,\mathbf{k},n}^\dagger d_{\eta,\mathbf{k},n} \varepsilon_{\eta,\mathbf{k},n} + \Phi_0 \sum_j d_{\eta,\mathbf{k},n}^\dagger d_{\eta,\mathbf{k}\pm M_j,n} \right), \quad (\text{S17})$$

where  $d_{\eta,\mathbf{k},n}^\dagger$  are creation operators in the band basis of the noninteracting Hamiltonian (S2), with eigenenergies  $\varepsilon_{\eta,\mathbf{k},n}$ . Here  $n$  is the band index, and momentum  $\mathbf{k}$  is restricted to the reduced Brillouin zone associated with the broken translational symmetry of the CDW order.

Figure S1 plots the density of states found from (S17), with  $\Phi_0 = 4$  meV, which provides a simple demonstration that the presence of the DW acts to split the moiré bands, generating many additional van Hove singularities. This provides a natural explanation for the additional features seen in the Hall number at low temperature, see Fig. 1e-g and Fig. 3c.

**Intervalley coherent DWs.** As alluded to in the main text, the measurements are not only consistent with simple CDW phases as defined above, but also with more exotic DW phases, as we will illustrate next. As spin-rotation invariance is already broken by the induced SOC, let us focus on states where real-space translations are intertwined with  $U(1)_v$ , the group of independent  $U(1)$  phase transformations in the two valleys. In that case, Eq. (S13) is replaced by

$$H_\Phi = \sum_{\mathbf{R} \in \text{ML}} \sum_{\eta,s,\alpha} \sum_{j=1}^3 \sum_{j'=1,2} \Phi_{j,j'} \cos(\mathbf{M}_j \mathbf{R}) c_{\mathbf{R},\alpha,\eta,s}^\dagger (\eta_{j'})_{\eta,\eta'} c_{\mathbf{R},\alpha,\eta',s}. \quad (\text{S18})$$

Here, the underlying order parameter is a real-valued  $3 \times 2$  matrix  $\Phi$  or, equivalently, three 2-component real vectors  $\varphi_j$  with  $(\varphi_j)_{j'} = \Phi_{j,j'}$ . Under  $U(1)_v$ , these vectors transform as  $\varphi_j \rightarrow e^{i\eta_v \varphi} \varphi_j$ , while  $\varphi_j$  transform the same way as  $\phi_j$  in Eq. (S13) under  $C_{3z}$  and translations. One difference is that they transform non-trivially under  $C_{2z}$ ,  $\varphi_j \rightarrow -\eta_z \varphi_j$ .

With these constraints, it is easy to show that the most general free-energy expansion reads as

$$\mathcal{F} \sim a(T) \sum_j \varphi_j^2 + c_1 \left( \sum_j \varphi_j^2 \right)^2 + c_2 \sum_{j_1 \neq j_2} (\varphi_{j_1} \cdot \varphi_{j_2})^2 + c_3 \sum_{j_1 \neq j_2} \varphi_{j_1}^2 \varphi_{j_2}^2. \quad (\text{S19})$$

Note that, as opposed to Eq. (S14), no third-order term is possible, which is a consequence of  $U(1)_v$ . The free energy in Eq. (S19) allows for the following four phases: two of them,

$$\varphi_1 = \varphi, \quad \varphi_{2,3} = 0 \quad (\text{S20})$$

and

$$\varphi_1 = \varphi, \quad \varphi_2 = \hat{z} \times \varphi, \quad \varphi_3 = 0. \quad (\text{S21})$$

are nematic, i.e., break  $C_{3z}$  symmetry and are, hence, less natural candidates than the  $C_{3z}$  preserving phases with

$$\varphi_j = \varphi \quad (\text{S22})$$

and

$$\varphi_j = (C_{3z})^{j-1} \varphi. \quad (\text{S23})$$

respectively.

For instance, the state defined by Eq. (S22) corresponds to a coupling (choosing  $\varphi = e_x$  for concreteness)

$$H_\Phi = \sum_{\mathbf{R} \in \text{ML}} \sum_{\eta, s, \alpha} \Phi(\mathbf{R}) c_{\mathbf{R}, \alpha, \eta, s}^\dagger(\eta_1)_{\eta, \eta'} c_{\mathbf{R}, \alpha, \eta', s}, \quad \Phi(\mathbf{R}) = \sum_{j=1}^3 \cos(\mathbf{M}_j \mathbf{R}). \quad (\text{S24})$$

The impact of DW order of this form on the band energies will be similar to that of a simple CDW as in Eq. (S17). However, since the resulting mini bands will be time-reversal symmetric superpositions of two valleys, sequentially filling these mini bands will always lead to DW states with vanishing Chern number, irrespective of the Chern numbers of the SOC coupled bands (cf. Fig. 2c of the main text, where we show one possible distribution of these Chern numbers). Further measurements are required, though, to be able to determine which of the different DW states is realized in the system.

### SI 3: twist angle and moiré filling

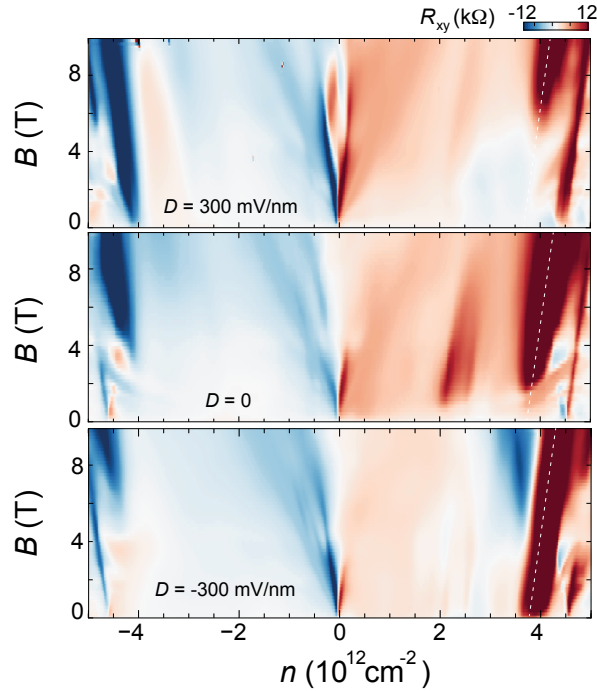


FIG. S2. **Landau Levels** Hall Resistance  $R_{xy}$  as a function of magnetic field  $B$  and carrier density  $n$  at  $T = 20$  mK. The measurements in the top, middle and bottom panels are performed at  $D = +300, 0$  and  $-300$  mV/nm, respectively.

**Sample A:** Fig. S2a shows the most prominent Landau fan away from the CNP, which are marked by the white dashed lines. We identify the zero field position of the white dashed lines as  $\nu_{TLG} = +4$ . The position of  $\nu_{TLG} = +4$  allows us to determine the twist angle to be  $\theta = 1.25^\circ$ . At  $D = 0$  the Landau fan emerging from the band gap is only stable at  $B > 2$  T, which is likely due to the influence of the monolayer band. In addition, the energy gap at both  $\nu_{TLG} = \pm 4$  can be revealed by the robustness of the Landau fan emerging from that density. The  $D$  dependence of the Landau fan, hence the robustness of the energy gap, exhibits the same behavior as shown in Fig. S5. The Landau fan at  $\nu_{TLG} = +4$  ( $-4$ ) becomes less (more) robust with increasing displacement field  $D$ .

Notably, the twist angle can be independently determined based on the magnetic field value of the high symmetry point in the Hofstadter spectrum, since the horizontal dashed lines in Fig. 2 correspond to integer values of  $\phi_0/\phi$ . Assigning the high symmetry point around  $B = 4.85$  T as  $\phi_0/\phi = 4$  gives rise to a twist angle of  $\theta = 1.22^\circ$ , which is consistent with the twist angle determined from the Landau fan. Fig. S3b plots Hall conductance  $\sigma_{xy}$  as a function of  $B$  and  $\nu_{TLG}$  at different  $D$ . The high symmetry point of the Hofstadter spectrum, which is marked by the horizontal

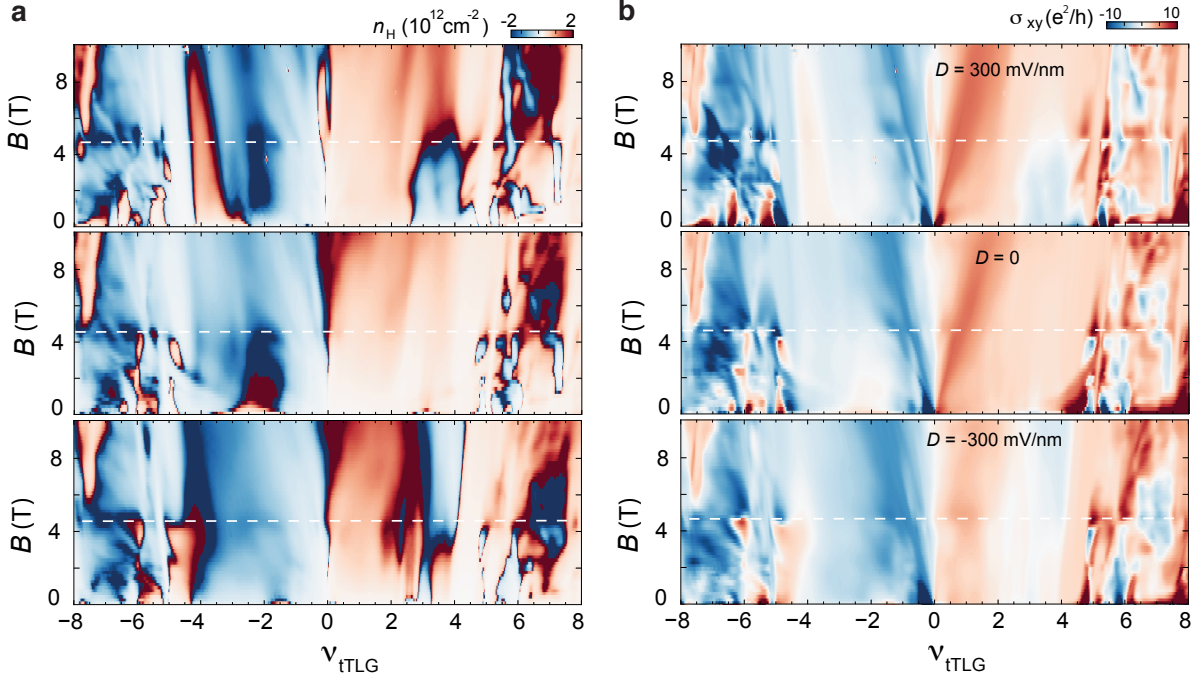


FIG. S3. **High symmetry point in the Hofstadter spectrum** (a) Hall density  $n_H$  and (b) Hall conductance  $\sigma_{xy}$  as a function of  $B$  and filling fraction  $\nu_{tTLG}$  at  $T = 20$  mK. The measurements in the top, middle and bottom panels are performed at  $D = +300, 0$  and  $-300$  mV/nm, respectively. The white dashed lines indicate the magnetic field in which there is one magnetic flux per 8 moiré unit cells

white dashed lines, is independent of  $D$ , suggesting that the moiré wavelength is the same between top/middle and middle/bottom graphene layers. In another word, the tTLG sample has a A-tw-A stacking order [11].

**Sample B:** in sample B, BLG and tTLG are separated by a WSe<sub>2</sub> crystal with thickness of 5 nm, as shown in Fig. S4. The edge of the flatband is determined by the position of resistance peak at  $\nu_{tTLG} = \pm 4$  in Fig. S4b. Measured along the red dashed line in Fig. S4b, the most prominent Landau fans emerge from  $\nu_{tTLG} = \pm 4$ , indicating new fermi surface emerge at this density, which offers further confirmation that  $\nu_{tTLG} = \pm 4$  marks the energy gap between the flat and remote bands. The dominating sequence of incompressible states have slope of  $\pm 2, \pm 6$  and  $\pm 10$ ... This suggests that the band structure of tTLG/WSe<sub>2</sub> can be viewed as a monolayer band plus a twisted bilayer flatband, which is consistent with previous observations in tTLG without proximity effect [9, 10, 41].

It is important to note that the Landau fan emerging from  $\nu_{tTLG} = +4$  is only observed at  $B > 2$  T, indicating that the ground state at  $\nu_{tTLG} = +4$  is not insulating at  $B = 0$ . This finite density of state within the moiré energy gap is likely due to the presence of the Dirac band from monolayer graphene. In the  $n\nu_{tTLG} - D$  map, the resistance peak at  $\nu_{tTLG} = \pm 4$  both show strong  $D$ -dependence. For example, the peak in  $R_{xx}$  at  $\nu_{tTLG} = +4$  disappears at  $D > -200$  mV/nm. Such  $D$ -dependence suggests that displacement field modifies the hybridization between the monolayer band and twisted bilayer band in a way that is asymmetrical in  $D$ . This is not surprising owing to the asymmetrical geometry of the tTLG/WSe<sub>2</sub> heterostructure. Most importantly, the band structure tTLG/WSe<sub>2</sub> heterostructure could be highly tunable with  $D$ . The energy gap at  $\nu_{tTLG} = \pm 4$  can be directly probed using chemical potential measurement, which reveal a  $D$ -dependence that is consistent with the  $\nu_{tTLG} - D$  map. At  $\nu_{tTLG} = +4$  ( $-4$ ), the energy gap between the flat and remote bands decreases (increases) with increasing displacement field  $D$ .

We note that Landau fans are observed in the remote band of sample B, which is consistent with the behavior of sample A (Fig. 2). Fig. S4 shows that the extra Landau fans in the remote band coincides with resistance peaks in  $R_{xx}$  and extra features in the Hall density  $n_{Hall}$ . However, we do not observe robust DWs within the flatband in sample B. This could be for two reasons: (i) DW states are stabilized by strong Coulomb correlation, the adjacent BLG in sample B introduces strong Coulomb screening that reduces Coulomb correlation strength, thus suppressing DWs in the moiré flatband; (ii) the twist angle of sample B ( $1.35^\circ$ ) is slightly larger compared to sample A ( $1.25^\circ$ ), and DW is stable in the smaller twist angle range; (iii) the sample is not uniform enough to resolve resistance features with a density modulation of  $1/4$  moiré filling. Notice that correlation-driven insulators are more robust in the remote band (Fig. 3), which may explain their presence in the remote band of sample B despite the presence of Coulomb

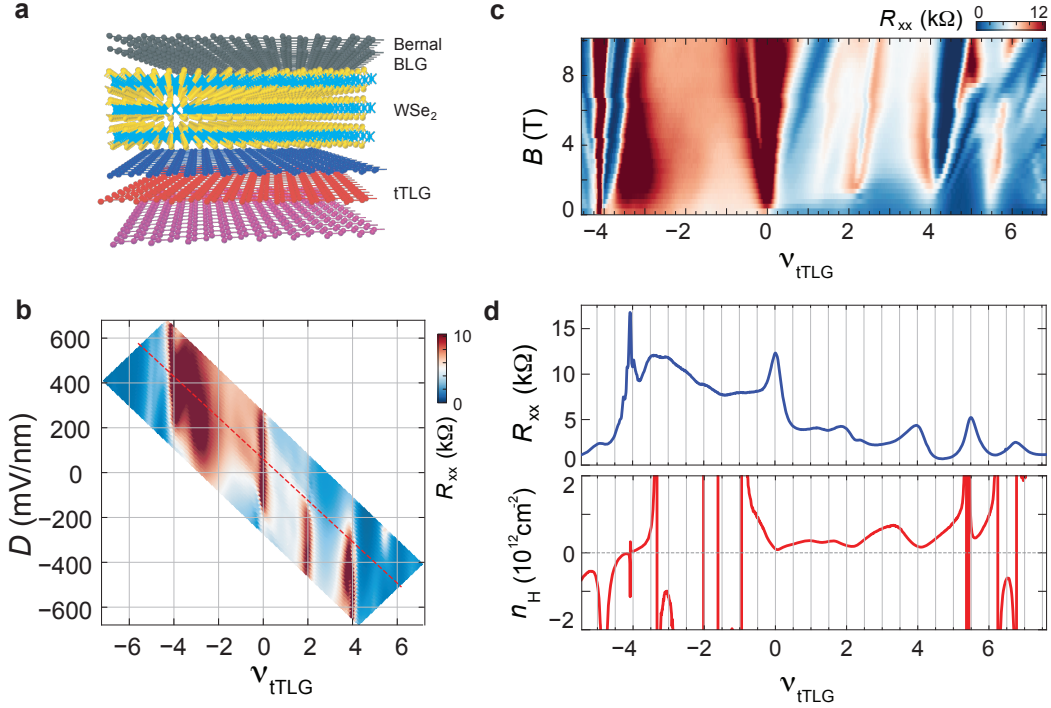


FIG. S4. **Sample B** (a) Schematic of sample B, where BLG and tTLG are separated by a WSe<sub>2</sub> crystal with thickness of 5 nm. (b) Longitudinal Resistance  $R_{xx}$  as a function of filling fraction  $\nu_{tTLG}$  and displacement field  $D$  measured at  $B = 0.4$  T and  $T = 20$  mK. (c)  $R_{xx}$  as a function of  $\nu_{tTLG}$  and  $B$  measured along the red dashed line in (b). (d)  $R_{xx}$  and hall density  $n_H$  as a function of  $\nu_{tTLG}$  measured along the red dashed line in (b).  $R_{xx}$  is measured at  $B = 0$ , where as  $n_H$  at  $B = 0.4$  T.

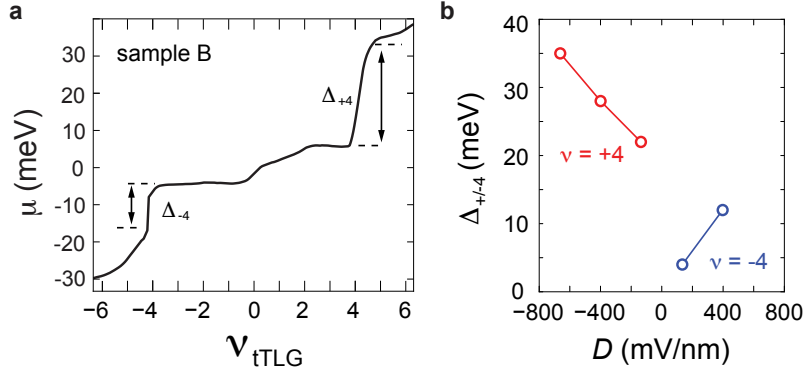


FIG. S5. **Sample B** (a)  $\mu_{tTLG}$  as a function of  $\nu_{tTLG}$  measured from sample B (same as Fig. 4a). Here we mark the jump in  $\mu_{tTLG}$  around  $\nu_{tTLG} = \pm 4$ , which correspond to the energy gap between the flatband and the remote bands,  $\Delta_{+4}$  and  $\Delta_{-4}$ . (b)  $\Delta_{+4}$  and  $\Delta_{-4}$  as a function of  $D$ .

screening.

Although Landau fans are observed emerging from  $\nu_{tTLG} = 1$  and 2, incompressible states associated with these Landau fans are only stable at  $B > 2$  T. The lack of correlated insulators at integer filling indicates that fermi surface reconstruction is not present at  $B < 2$  T. This is consistent with the lack of saw tooth pattern in the chemical potential measurement (Fig. 4a).

**Sample C:** sample C has twist angle of  $\theta = 1.50^\circ$ . The Landau fan measured from sample C exhibits two types of phenomena. Across the moiré flatband,  $-4 < \nu < +4$ , there is a clear hierarchy in the correlated phases: the most robust incompressible states are parametrized with integer values in the intercept  $s$ . More importantly, the slope  $t$  of the most prominent incompressible states exhibits a unique correlation with  $s$  which is consistent with previous observation in graphene moiré structures without the proximity effect [50, 51]: for  $s = \pm 1$  ( $\pm 2$ ), the most

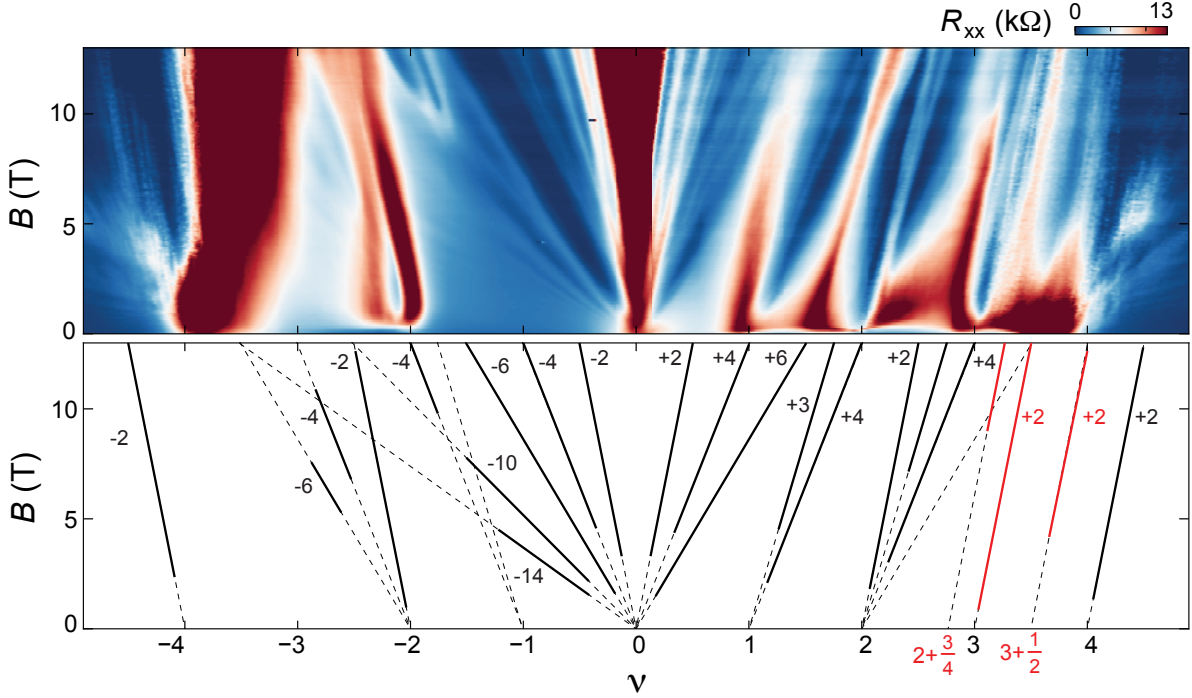


FIG. S6. **Landau fans in sample C** (top panel) Longitudinal resistance  $R_{xx}$  as a function of magnetic field  $B$  and moiré filling  $\nu$  measured at  $T = 20$  mK and  $D = 0$  in sample C, which has a twist angle of  $\theta = 1.5^\circ$ . (bottom panel) Schematic Landau fan capturing the most prominent incompressible states in the Landau fan. Around the charge neutrality point, the Landau fan exhibits similar behavior compared to magic-angle tTLG without proximity [41]. The Landau fan emanating from the CNP has a main sequence of  $\pm 2, \pm 6, \pm 10 \dots$ . In addition, fermi surface reconstruction at integer filling appears to play a dominating role, as extra Landau fans emerge from  $\nu = \pm 1, \pm 2 \dots$ . These reconstructed fermi surface provides strong indication for TI-FSB at integer fillings. In the filling fraction range  $2 < \nu < 4$ , the behavior of the Landau fan deviates from that of magic-angle graphene moiré. In this range, the most robust incompressible states are all parametrized with slope  $t = +2$ . At the same time, we observe a series of incompressible states with fractional intercept of  $s = 2 + 3/4$  and  $3 + 1/2$ . It is worth pointing out that the incompressible state emerging from  $\nu = +3$  is expected to have a slope of  $t = 1$  when TI-FSB is the dominating symmetry breaking mechanism [50, 51]. The unique slope and intercept observed in sample are similar to observations in sample A, which point towards a symmetry breaking mechanism different from TI-FSB. This new mechanism is likely realized through the proximity effect across the tTLG/WSe<sub>2</sub> interface.

prominent incompressible state has a slope of  $\pm 3$  ( $\pm 2$ ), which corresponds to a quantized Hall conductance of  $\pm 3 \frac{e^2}{h}$  ( $\pm 2 \frac{e^2}{h}$ ). This unique hierarchical behavior in the value of  $s$ , combined with the correlation between  $s$  and  $t$ , points towards the mechanism underlying spontaneous symmetry breaking in graphene moiré systems, which gives rise to TI-FSB. Remarkably, a different type of behavior is observed in the filling range  $2 < \nu < 4$  in sample C. In this range, incompressible states are all parametrized with  $t = +2$ , independent of the intercept  $s$ . At the same time, incompressible states with  $s = 3 + 1/2$  and  $2 + 3/4$  are observed (marked by red solid lines in Fig. S6). Such behavior is similar to the 2-unit-cell and 4-unit-cell states observed in sample A. As alluded to in the maintext, the DW states is stabilized by a mechanism that is distinct from TI-FSB. In addition to the influence of the proximity effect, the fact that both TI-FSB and DW instability are present in sample C points towards the influence of twist angle.

**Comparison between sample A, B and C:** in the following, we will compare transport behavior between different samples. The  $\nu_{tTLG} - D$  map reveals a few similarities: (i) areas with large resistance are observed near  $\nu_{tTLG} = \pm 4$ , which corresponds to the transition between the flat and remote energy bands; (ii) areas with low resistance are observed outside of  $\nu_{tTLG} = \pm 4$ , which points towards a highly compressible ground state outside of the flat band; (iii) in both samples, the resistance peaks near  $\nu_{tTLG} = \pm 4$  exhibit  $D$  dependence and the peak value is asymmetric in  $D$ ; (iv) an abundance of correlated insulators are observed in the remote bands of both samples. The fact that  $1/4$  DW states are not observed in sample B could result from several possibilities: (i) the influence of Coulomb screening; (ii) the larger twist angle and (iii) sample inhomogeneity.

$R_{xx}$  and Hall density as a function of  $\nu_{tTLG}$  offers a another direct comparison between the two samples. For both samples, an abundance of vHSs are observed in the hole doped flatband, as well as the remote band.  $n_H$  lack density

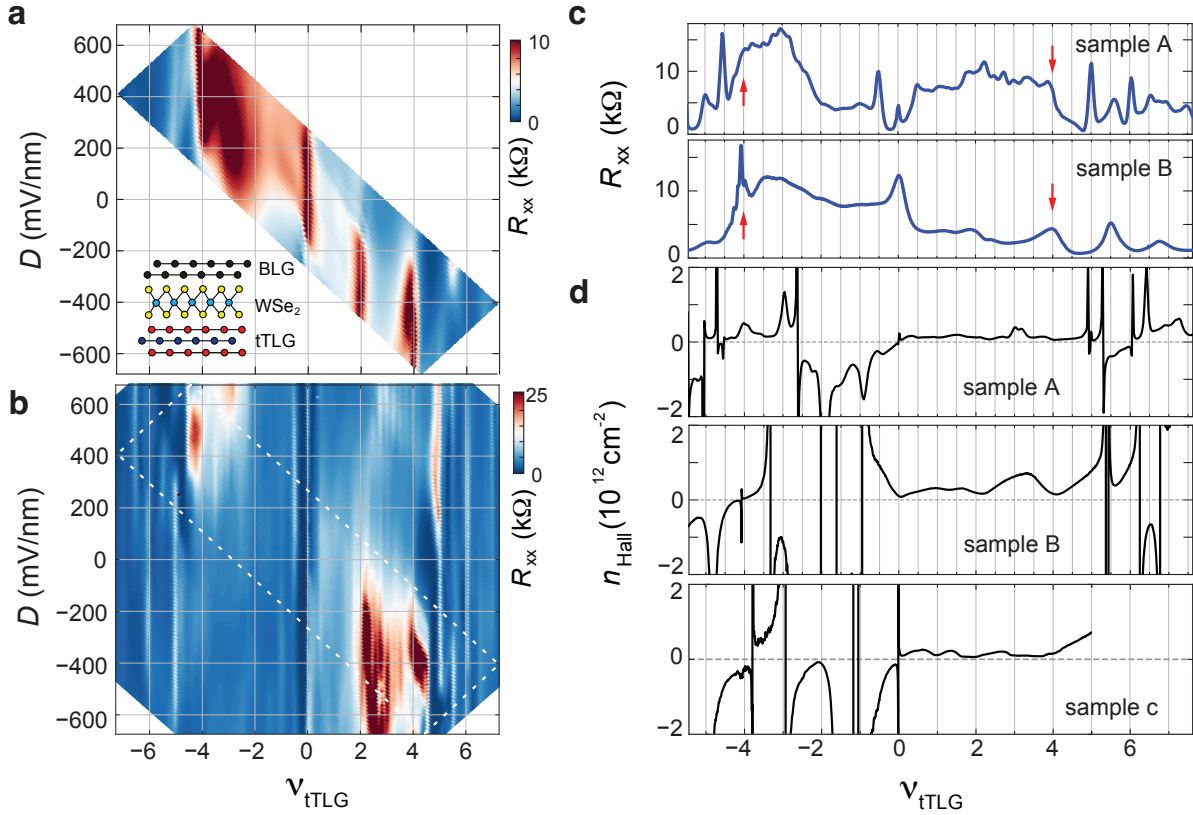


FIG. S7. **Sample A, B and C** Longitudinal Resistance  $R_{xx}$  as a function of filling fraction  $\nu_{tTLG}$  and displacement field  $D$  for (a) sample A (b) sample B. The white dashed line in (b) marks the boundary of the area mapped in (a). For sample A, the area of the phase space is limited by interlayer tunneling across the WSe<sub>2</sub> crystal. (c)  $R_{xx}$  and (d)  $n_H$  as a function of  $\nu_{tTLG}$  measured from (top panel) sample A and (bottom panel) sample B. Measurements are performed at  $T = 20$  mK and  $B = 0.4$  T.

dependence in the electron doped flatband of sample A, which reflects the influence of DW instability. Interestingly,  $n_H$  shows similar behavior in sample B, which could indicate that DW instability is emerging, albeit very weak, in the flatband of sample B. In Fig. S7c, red arrow marks the position where Landau fan emerges. For both samples, the resistance background drops significantly at the position of the red arrow, which offers another indirect indication for the transition between the flat and remote energy bands.

Fig. S7d compares the Hall density  $n_H$  as a function of moiré filling. In all three samples, the flatband with electron doping shows little variation in  $n_H$ . On the other hand, a series of vHSs are observed in the hole doping band. The fact that all three samples show similar behavior in  $n_H$  offers strong indication for the influence of proximity effect across the tTLG/WSe<sub>2</sub> interface. We note that the behavior of  $n_H$  shown in Fig. S7d is distinct from graphene moiré systems without proximity effect. This could be consistent with the scenario where fermi surface is reconstructed by the influence of the underlying symmetry breaking mechanism.

**Influence of  $D$ :** owing to the excellent sample quality, sharp resistance features in sample A can be resolved with high resolution. This allows us to examine the influence of  $D$  on the energy band structures. Fig. S8 examines the behavior of the Landau fan emerging from  $\nu_{tTLG} = 4$  at different  $D$ . Apart from the apparent  $D$ -dependence where the Landau fan weakens with increasing  $D$ , Fig. S8c-d, g-h show that the incompressible state with a slope of +2 consist of multiple features. This is similar to the behavior shown in Fig. 2d-f, where a series of incompressible states appear with the same slope  $t$  but different intercept  $s$ . Fig. S9 offers a direct demonstration of this phenomenon, where multiple incompressible states appears near  $\nu = -4$  with a density modulation of  $1/8$  moiré filling in the valley of  $s$ .

Notably, the position of the Landau fan emerging from  $\nu_{tTLG} = 4$  can be influenced by  $D$ . It shifts by  $1/4$  filling between  $D = -300$  and  $-400$  mV/nm (Fig. S8d-e, h-i). The fact that the shift is a fractional moiré filling suggests that the transition between the flat and remote energy bands is influenced by DW instability. Although we do not fully understand this behavior, this observation could naturally result from the complex interaction between multiple

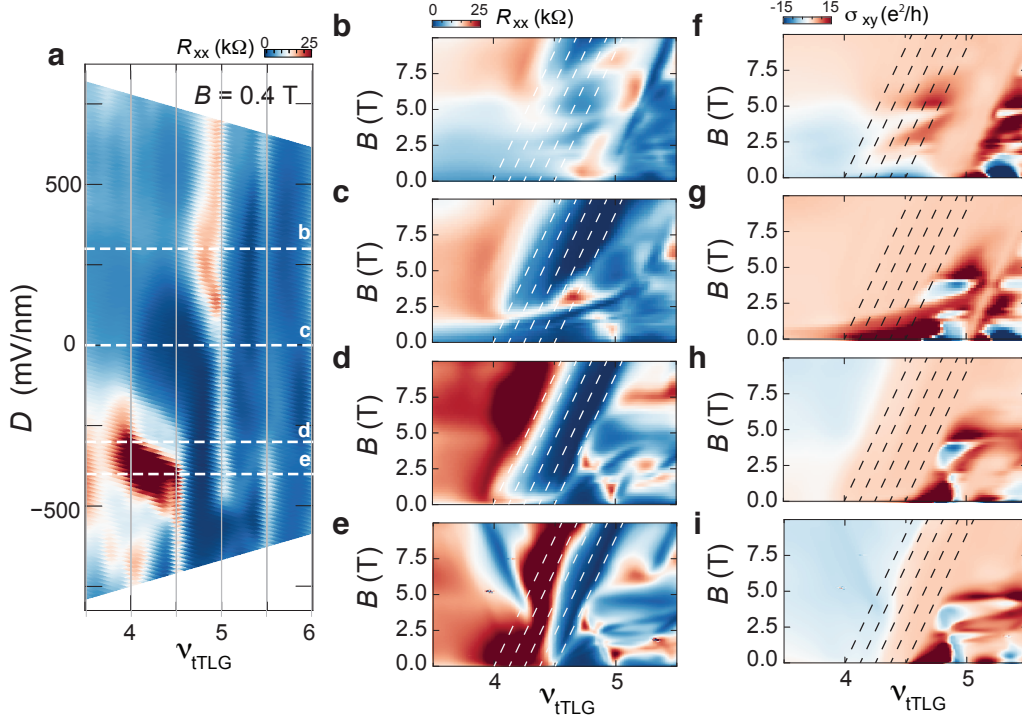


FIG. S8. **Shifting in  $\nu = 4$  state.** (a) Longitudinal resistance  $R_{xx}$  as a function of displacement field  $D$  and filling fraction  $\nu_{tTLG}$  on the electron-doped side. (b - e) Longitudinal resistance  $R_{xx}$  as a function of magnetic field  $B$  and filling fraction  $\nu_{tTLG}$  taken at (b)  $D = 300$  mV/nm (c)  $D = 0$  mV/nm (d)  $D = -300$  mV/nm (e)  $D = -400$  mV/nm. (f - i) Hall conductance  $\sigma_{xy}$  as a function of magnetic field  $B$  and filling fraction  $\nu_{tTLG}$  taken at (f)  $D = 300$  mV/nm (g)  $D = 0$  mV/nm (h)  $D = -300$  mV/nm (i)  $D = -400$  mV/nm.

energy bands near the transition between the flat and remote bands, as shown in Fig. 4d. Varying  $D$  also modifies the hybridization between the flat bilayer band and the more dispersive monolayer band.

We note that such  $D$  dependence is also observed in the superconducting phase at  $B = 0$  [39]. This offers an intriguing opportunity to compare the influence of  $D$  on the underlying band structure and the stability of superconductivity. Such comparison promises to shed light on the origin of the superconductivity. Fig. 3b shows that the vHS at  $\nu = 4.5$  and low temperature shifts back towards  $\nu = 4$  at  $T = 10$  K. This temperature dependence confirms that the  $D$ -induced shift in the Landau fan at low temperature is Coulomb-driven. As the influence of Coulomb correlation diminishes at higher temperature, the shift disappears as well.

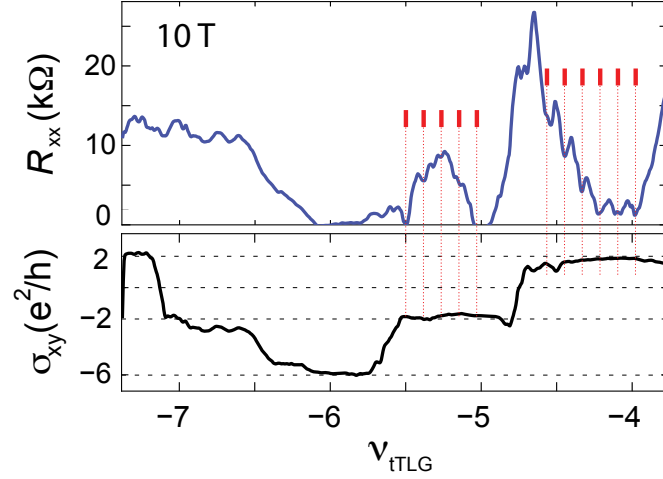


FIG. S9. **Degeneracy of incompressible states**  $R_{xx}$  (top panel) and  $\sigma_{xy}$  (bottom panel) as a function of  $\nu_{tTLG}$  measured at  $D = 500$  mV/nm,  $B = 10$  T and  $T = 20$  mK. Over most of the density range in the remote band, incompressible states have Hall resistance plateau with quantization value of  $\pm 2, \pm 6 \dots$ . The sequence of incompressible states reveals that fermi surface resulting from DW instability resembles that of Dirac cones. At the same time, they inherit the 4-fold degeneracy. One natural interpretation is that the interaction-reduced band reconstruction leads to revival of the Dirac cones in the remote bands at those fillings, possibly similar to that in twisted bilayer graphene [12], while retaining the valley and spin flavor symmetry.

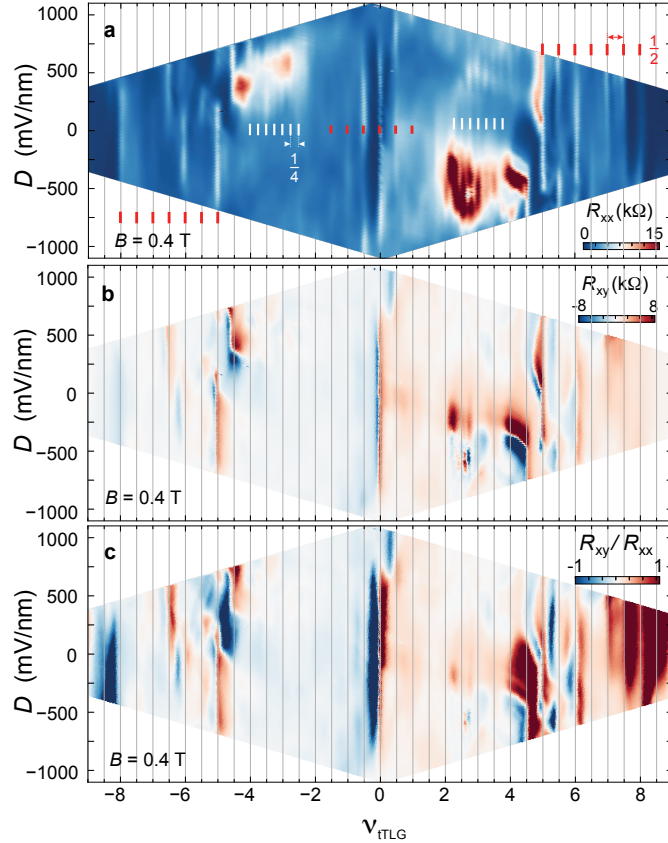


FIG. S10. **Transport anisotropy** (a) Longitudinal resistance  $R_{xx}$ , (b) Hall resistance  $R_{xy}$ , and (c) transport anisotropy  $R_{xy}/R_{xx}$  as a function of displacement field  $D$  and filling fraction  $\nu_{tTLG}$  measured at  $T = 20$  mK and  $B = 0.4$  T. Strong transport anisotropy is observed near the CNP and in the remote band, which are portions of the phase space occupied by the  $1/2$  DW states. No obvious anisotropy is observed to be associated with the  $1/4$  DW states.

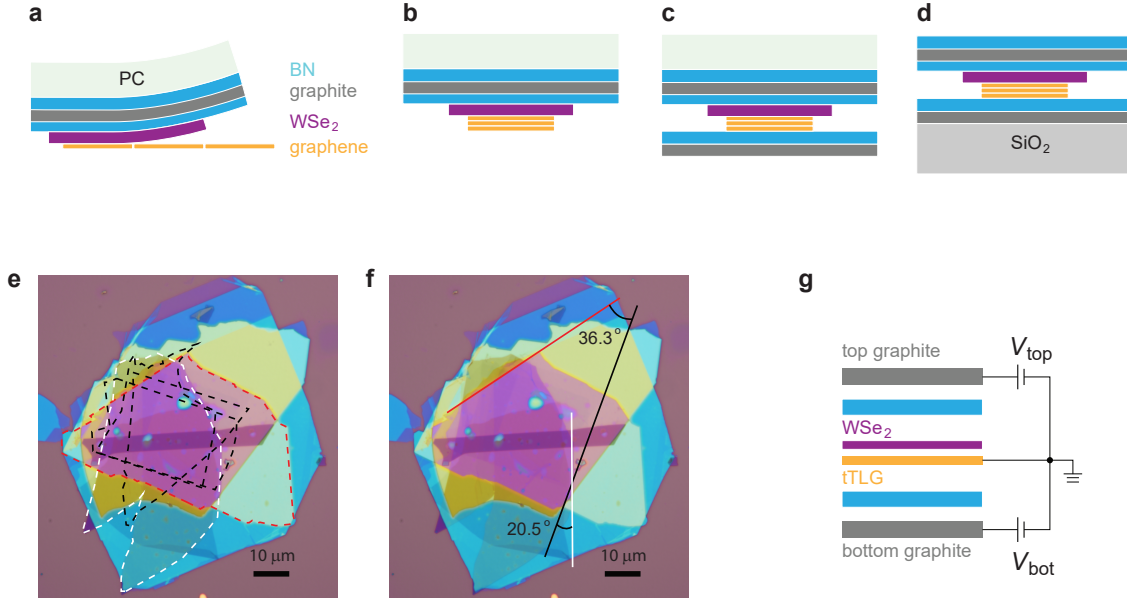


FIG. S11. **Fabrication of the sample.** (a-d) Schematics for stacking tTLG with cut-and-stack technique. (e) The optical image of the sample. The black dashed line, white dashed line, and red dashed line represent the boundary of graphene, WSe<sub>2</sub>, and bottom BN respectively. (f) The alignment of each crystal. The optical image shows the angle between graphene and WSe<sub>2</sub> to be 20.5 °, and the angle between graphene and bottom BN to be 36.3 °. (g) The schematic of the device with the gate-controlled voltage

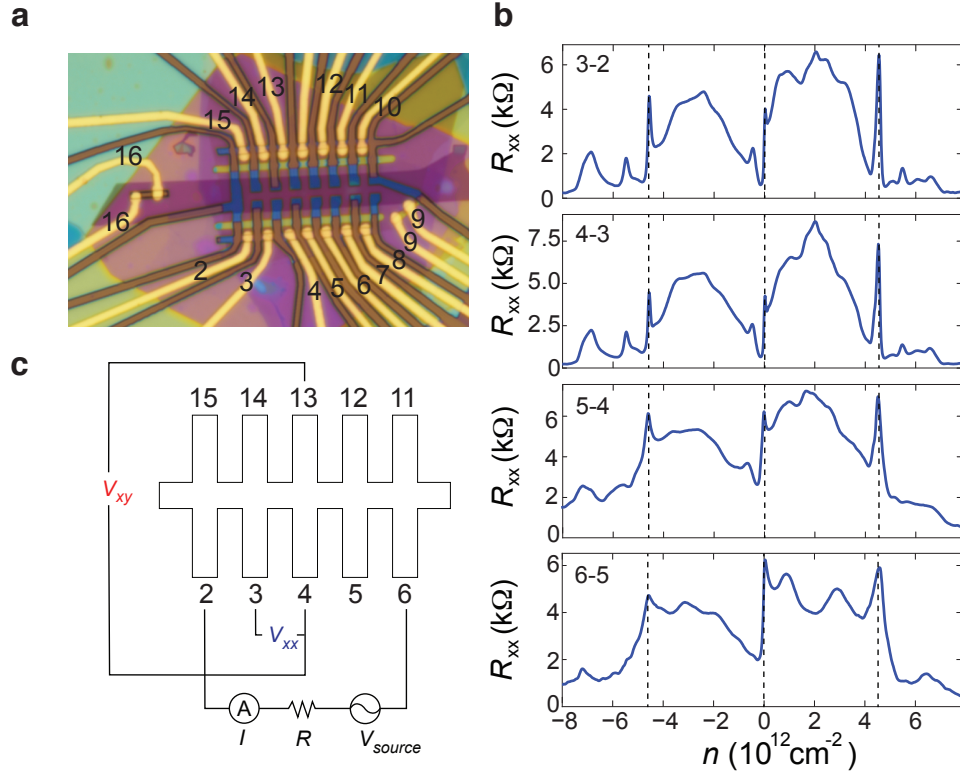


FIG. S12. **Two-terminal measurement.**(a) an optical image of the sample with labeled lead. (b) The two-terminals measurement at different pin with  $D = 0 \text{ mV/nm}$ . The current source and sink is placed on pin 10 and 15 respectively. Within the pin range from 2-6, the longitudinal resistances show matching peak, confirming in twist-angle homogeneity in the region.(c) the schematic of the four-terminal measurement setup for the rest of the experiment where  $R_{xx} := V_{xx}/I$  and  $R_{xy} := V_{xy}/I$ .

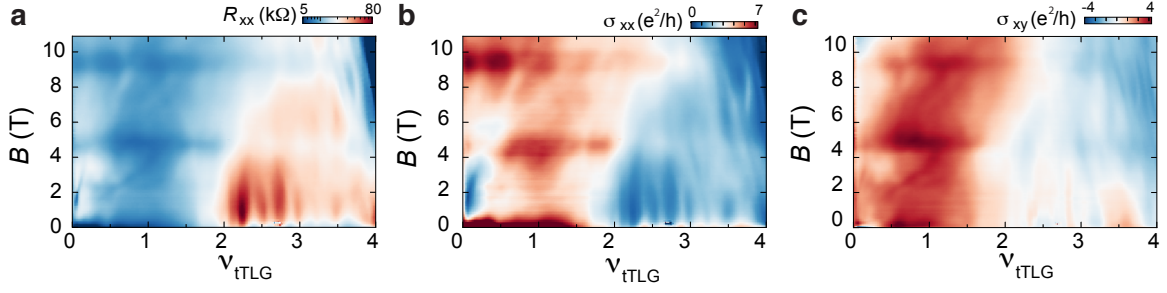


FIG. S13. **Density waves at negative displacement field** (a) Longitudinal resistance  $R_{xx}$  (b) Longitudinal conductance  $\sigma_{xx}$  (c) Hall conductance  $\sigma_{xy}$  as a function of filling fraction  $\nu_{tTLG}$  and magnetic field  $B$ .

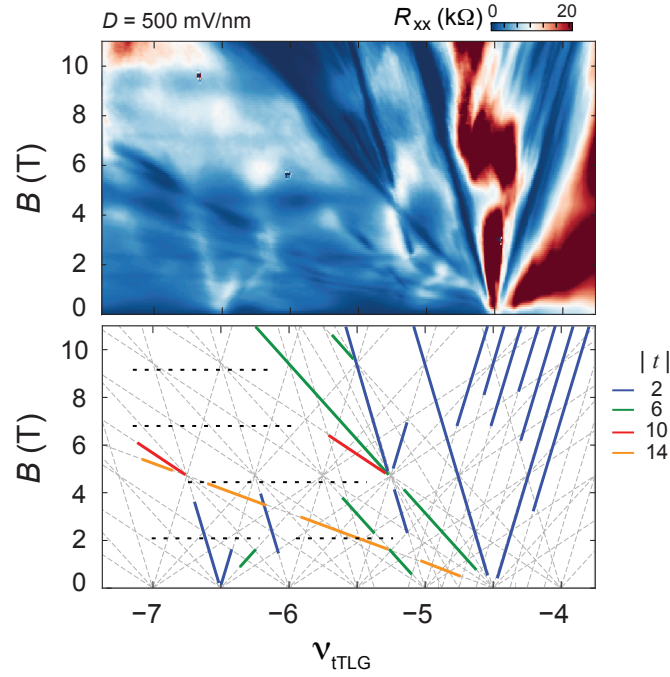


FIG. S14. **Degeneracy of incompressible states** (a)  $\nu_{tTLG} - B$  map of  $R_{xx}$  measured at  $D = 500$  mV/nm. (b) Schematic summarizing the most prominent features in panel (a). Incompressible states are color coded according to their slope  $t$ . Blue, green, red and orange solid lines denote incompressible states with slope  $t = \pm 2, \pm 6, \pm 10$  and  $\pm 14$ , respectively.